



**Industrial Group Project 2021**  
**School of Physics**

Authors	Daniel Elston, Hannah Worth, Samuel Flowers, Joshua Sinclair
Academic Supervisor	Dr Sudarshan Paravamesvaran
Title	Fast Beam Loss Monitor for Rapid Deployment at the LHC
Date of Submission	29/04/2021
Word Count	11938

## Declaration

We were unable to collect any data in a laboratory setting due to the impact of COVID-19 regulations. Hereby, all data within this report has been taken from component data sheets or referenced academic sources, with further analysis and calculations taking place in lieu of experimental results. This report was completed entirely by the four authors listed above, supervised by Dr Sudarshan Paravamesvaran, and in collaboration with the industrial client at CERN: Dr James Storey. The introduction and theoretical background sections of this report draw heavily upon the knowledge contained in the literature reviews submitted in November 2020, but with greater applied project specificity. All diagrams have been created by us, unless stated otherwise and appropriately referenced. The work put into the research carried out, along with the writing of the report has been split equally between the four participants in this group. The communications aspect of the project, relating to the organisation of client and supervisor meetings, and other necessary emailing, have been largely undertaken by Dan and Hannah.

## COVID-19

This project was extensively affected by COVID-19 and all the restrictions that came with it. We were unable to participate in any in-person meetings throughout the course of the year, forcing us to instead collaborate regularly over Zoom and Microsoft Teams. This had a huge impact on the overall ability to communicate within the group, especially on highly technical or theoretical matters where the ability to physically illustrate something is as invaluable as it is irreplaceable, using online group work software. Consequently, we found that this group project required a lot more independent work, often leaving us feeling out of sync and having to struggle through technicalities alone due to the more strict division of labour and component research that needed to be implemented in comparison to a normal year. Over the course of the year, a substantial amount of meeting time has also been lost due to technical difficulties, such as internet connection failures. This has hindered the momentum and efficiency of meetings, and the already limited time we have been able to verbally communicate with each other. Additionally, the third UK national lockdown made it impossible to go into the laboratory and build our detector design, despite us having already met with Dr David Cussans and arranged the acquisition of the necessary components. Accordingly, we had to very quickly shift our report from being a classic experimental report to a more theoretical prototype, comparing expected values against pre-existing BLM systems, due to our inability to collect any experimental data whatsoever ourselves. Upon discussion with the client and supervisor, it was decided that the report should diverge from the recommended structure in the industrial group project handbook; by switching around the methods and results section to accommodate for the lack of results, and shift the focus of the project towards theory and analysis.

## Strikes

This project was not at all affected by any university strikes.

Project Report presented as part of, and in accordance with, the requirements for the Final Degree of BSc at the University of Bristol, Faculty of Science

We hereby assert that we own exclusive copyright in the item named below. We give permission to the University of Bristol Library to add this item to its stock and to make it available for consultation in the library, and for inter-library lending for use in another library. It may be copied in full or in part for any bona fide library or research worked, on the understanding that users are made aware of their obligations under copyright legislation, i.e. that no quotation and no information derived from it may be published without the consent of the prior authors.

Authors	Daniel Elston, Hannah Worth, Samuel Flowers, Joshua Sinclair
Title	Fast Beam Loss Monitor for Rapid Deployment at the LHC
Date of Submission	29/04/2021

Signed: Samuel Flowers, Daniel Elston, Hannah Worth, Joshua Sinclair

Date: 29/04/2021

This project is the property of the University of Bristol Library and may only be used with due regard to the rights of the author. Bibliographical references may be noted, but no part may be copied for use or quotation in any published work without the prior permission of the author. In addition, due acknowledgement for any use must be made.

## Acknowledgements

We would like to warmly express our gratitude to Dr Sudarshan Paravamesvaran for providing constant guidance and solutions throughout this project, particularly with regard to the sudden changes necessary due to COVID-19. In addition, we'd like to show our unending appreciation to Dr James Storey for providing insight into the technical workings of CERN, his extensive knowledge of beam loss monitoring, and for enthusing us with his love of the subatomic. An additional massive thank you to Dr David Cussans who took the time to discuss component technicalities in detail with us, providing invaluable expertise of the practical challenges faced by particle detection systems. This project was made possible by their kind words, imparted wisdom, patience and professionalism.

## Executive Summary

The Large Hadron Collider is the world's largest particle accelerator, located at CERN, Geneva. When particle beams collide, high energy subatomic particles can deviate from their superconducting magnet-guided paths. This loss of energy is known as 'fast beam loss'. When these lost particles come into contact with the mechanical components of the accelerator, this can result in incredible damage. A large portion of the work at CERN goes into the design and maintenance of beam loss monitoring (BLM) systems. These BLM systems detect and identify lost particles, which allows a faulty beam to be discharged before it can cause any structural damage, in a process known as 'dumping'.

The aim of this project is to design and develop a prototype fast BLM system that can detect lost particles quickly enough to allow their removal, before damage can occur. There are essential specifications that the detector system is to fulfil, which were provided by the client at CERN and are discussed in section 1.3. The most important requirement of any detector device is a time resolution of less than 25 ns, and detection rate of up to  $1 \times 10^6$  minimum ionising particles per second to allow for the tracking of particle bunches. The detector itself must be able to be quickly installed into and able to withstand the radiation environment of the LHC tunnel and is required to have a surface area greater than  $1 \text{ cm}^2$ . In addition, the budget for this design is given as 10,000 CHF.

Within sections 1 and 2, the importance of beam loss monitoring at the LHC, along with a review of different types of detector systems and their capabilities are discussed. The scene is set by first reviewing the processes that occur when charged particles travel through matter, and the energy that is dissipated in doing so. An understanding of this process is fundamental to developing a system which can detect and distinguish between high energy particles. Section 3 then gives a detailed overview of the proposed detector setup and its physical capabilities, through an explanation of the physics behind each component, as well as an evaluation of the cost. The detector type chosen was a plastic scintillator detector, connected to a photomultiplier tube (PMT) and read using the optical fibre network at CERN.

The expected performances of the prototype setup chosen are stated in section 4. These calculations were completed using relevant textbooks, reports on similar BLM systems and values obtained from the specific component data sheets. The overall time resolution of the detector is calculated to be 35 ps, with the ability to measure 1 and  $1 \times 10^6$  minimum ionising particles in 25.7 ns and 25.7  $\mu\text{s}$ , respectively. The total cost of our design is approximately 3650 CHF (not including readout), it has a surface area of  $1 \text{ cm}^2$  and can withstand a radiation dose of 1 kGy.

Section 5 gives an overview of the experimental methods that can be carried out to verify the expected performance of our prototype system, given in section 4. This then leads into a discussion in section 6 of the different ways to optimise the design, anticipated experimental difficulties, and a comparison of the chosen device against the Timepix3 hybrid pixel detector. A consideration of the read-out system necessary to carry the signal from our detector to the surface is also undertaken in section 6.7.

This report is therefore a prototype document, with the intention to provide an overview of fast beam loss monitoring, a BLM system design within the project requirements, and the experimental methods necessary to validate these expected capabilities.

# Contents

<b>1</b>	<b>Introduction</b>	<b>8</b>
1.1	The Large Hadron Colider . . . . .	8
1.2	The Importance of Beam Loss Monitoring . . . . .	8
1.2.1	Beam Loss Monitoring . . . . .	8
1.2.2	Types of Beam Loss . . . . .	8
1.2.3	Damages Caused by Fast Beam Loss . . . . .	9
1.3	Project Aims . . . . .	9
<b>2</b>	<b>Theoretical Background</b>	<b>9</b>
2.1	Interaction of Charged Particles with Matter . . . . .	9
2.2	Minimum Ionising Particles . . . . .	10
2.3	Key Principles of Fast Beam Loss Detection . . . . .	10
2.4	Current BLM Systems at CERN . . . . .	11
2.4.1	Ionisation Chambers . . . . .	11
2.4.2	Solid State Detectors . . . . .	11
<b>3</b>	<b>Prototype Detector Design</b>	<b>12</b>
3.1	Scintillation Detectors . . . . .	12
3.1.1	Inorganic Scintillators . . . . .	12
3.1.2	Organic Scintillators . . . . .	13
3.2	Signal Digitisation and Amplification . . . . .	14
3.2.1	Photomultiplier Tubes . . . . .	14
3.2.2	Photocathode . . . . .	14
3.2.3	Dynode Arrays and Signal Amplification . . . . .	15
3.2.4	Anode Readout . . . . .	16
3.2.5	Dark Current and its Minimisation . . . . .	16
3.3	Time Characteristics . . . . .	16
3.4	Final Prototype . . . . .	17
3.4.1	Scintillator . . . . .	17
3.4.2	Photo Multiplier Tube . . . . .	18
3.5	Necessary Experimental Accessories . . . . .	19
3.6	Cost Sheet . . . . .	19
<b>4</b>	<b>Expected Performance</b>	<b>19</b>
4.1	Detector Efficiency . . . . .	19
4.2	Theoretical Detection Results . . . . .	19
4.3	Operating Conditions . . . . .	20
4.4	Corrected System Rise Time . . . . .	20
4.5	Time Resolution for Bunch-by-Bunch BLM . . . . .	20
<b>5</b>	<b>Experimental Verification</b>	<b>20</b>
5.1	Component Setup . . . . .	20
5.2	Calibration of the Signal Digitisation System . . . . .	21
5.2.1	PMT Dark Noise Correction . . . . .	21
5.2.2	Coincidence Detection . . . . .	21
5.2.3	PMT Calibration Using a Pulse Generator . . . . .	21
5.3	Calibration of Scintillator Detector using Cosmic Rays . . . . .	21
5.4	Pulse Generator to Simulate LHC Bunches . . . . .	21
5.5	Optimal Conditions and Efficiency . . . . .	22
5.5.1	Minimum MIPs Detectable . . . . .	22
5.5.2	Maximum MIPs Detectable . . . . .	22
5.5.3	Effects of Magnetic Field . . . . .	22
5.5.4	Orientation . . . . .	22

<b>6</b>	<b>Discussion</b>	<b>22</b>
6.1	Evaluation of the Chosen Detection System Against Project Brief . . . . .	22
6.2	Maximum Efficiency and Theoretical Optimal Conditions . . . . .	22
6.3	Improving System Time Resolution . . . . .	23
6.4	Improving the Signal to Noise Ratio . . . . .	23
6.5	Radiation Hardness and Life Expectancy . . . . .	24
6.6	Critical Appraisal Against Current CERN Detectors . . . . .	24
6.7	Further Areas of Research . . . . .	25
<b>7</b>	<b>Conclusion</b>	<b>25</b>
<b>8</b>	<b>Appendix</b>	<b>26</b>
8.1	PMT Theoretical Calibration . . . . .	26
8.2	Efficiency Calculations . . . . .	26
8.3	Theoretical Detection Results . . . . .	26
8.4	Theoretical Detection Results With Maximum Efficiency Setup . . . . .	27
8.5	Corrected System Rise Time . . . . .	27
8.6	Time Resolution for Bunch-by-Bunch Beam Loss Measurements . . . . .	27

# 1 Introduction

## 1.1 The Large Hadron Collider

The Large Hadron Collider (LHC) is the world's largest and most powerful particle accelerator. It consists of a 27-kilometre ring tunnel of superconducting magnets that accelerate and collide subatomic particles. It first became operational on 10 September 2008, and remains the latest addition to CERN's accelerator complex [1].

The first collisions were achieved in 2010 at an energy of 3.5 TeV per beam, about four times the previous world record [1]. Since then, the LHC has broken numerous records and has resulted in countless ground-breaking discoveries. One of the most famous discoveries made at the LHC in recent years is the Higg's boson in 2012, which is a new elementary particle in the Standard Model [2].

The collider tunnel contains two adjacent parallel beam lines, which travel in opposite directions around the ring. High energy particle beams are guided around these accelerator rings by a strong magnetic field which is generated by superconducting electromagnets. These beams are then focused using collimators, which alter the cross-sectional area of the beam in a manner similar to an optical lens. The particles in the beams reach a velocity near the speed of light before they collide.

The main circular beam has four crossing points, around which are positioned seven detectors, each designed for different kinds of research as shown in figure 1. The ultimate aim of the LHC's detectors is to allow physicists to test the predictions of different theories of particle physics, and discover any unknown mechanisms or particles that exist in nature.

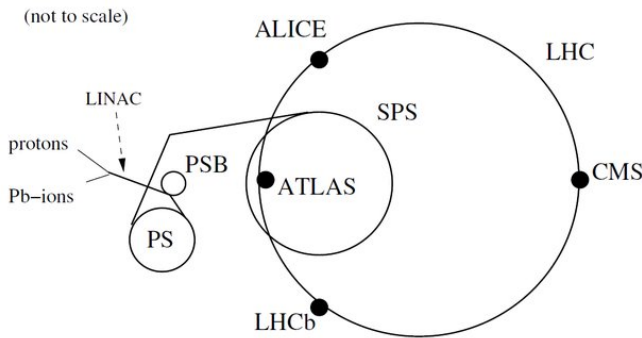


Figure 1: A basic diagram of the different experiments situated in the LHC [1].

The physical principles used at CERN are also extremely useful for other industrial applications. These include:

- Probing matter in biological and chemical research.
- Treating cancer with hadrons and radiotherapy in medicine.
- Scanning cargo in security.

- X-ray imaging.

to name but a few.

## 1.2 The Importance of Beam Loss Monitoring

### 1.2.1 Beam Loss Monitoring

Each beam in the LHC is accelerated to an energy of around 7 TeV [3]. If even a small fraction of this energy is erroneously discharged during the collision of two particle beams, it can therefore lead to devastating and expensive physical damage to the machine components of the accelerator.

A Beam Loss Monitoring (BLM) system is a series of interconnected detectors, like those shown in figure 2, which are placed around the LHC to detect beam loss and transmit data to a control room, so that the beam can be 'dumped' before stray particles can cause damage to machine components. A measurement of the position and magnitude of the loss pattern also makes it possible to determine which components caused the loss, and alter the beam infrastructure accordingly. Different BLM systems are used to detect beam losses of varying resolutions and sensitivities; this is discussed further in section 2.



Figure 2: An image of gas chamber beam loss detection systems placed around the main accelerator ring tunnel [4].

### 1.2.2 Types of Beam Loss

There are two main types of beam loss which are referred to as 'regular' and 'irregular'.

Regular beam loss refers to 'slow' beam losses. These are typically localised to the collimator or other aperture sections where the beam is focused. Regular beam losses show the lifetime of the beam and the transport efficiency of the beam accelerator, while it is being continuously operated during an experiment. This type of beam loss is not unexpected, and thus will not be the focus of this project.

An irregular beam loss, on the other hand, is referred to as a 'fast' or 'uncontrolled' loss. This type of beam loss typically occurs due to a misalignment of the beams being collided, or faulty accelerator elements. A well-designed collimator system might capture the majority of the losses, although a mere fraction of them can still cause damage at other locations [5].



### 1.2.3 Damages Caused by Fast Beam Loss

The maximum energy that can be locally deposited in a superconducting conducting magnet, without provoking transition of the whole superconducting coil to a normal conducting state, is called the 'quench level' [6]. The low temperature of the superconductors at can be lifted significantly as a result of these damages, which will lead to a loss of superconductivity and further beam containment in a chain-like effect.

Fast beam loss thus has the potential to destroy the beam pipe or collimator sections, and may break the vacuum seal enclosing the experiment as shown in figure 3. Therefore, any detector design needs to be able to detect the early stages of beam loss when there are only relatively few incident charged particles upon it. A low amount of energy should accordingly be set as the trigger of a beam dump, which will cut the chain reaction of damage short and prevent the magnets from quenching.

In the LHC, the total stored energy in a circulated beam reaches 392 MJ; while the quench level is of order of a few mJ/cm<sup>3</sup>, therefore a small loss of order  $1 \times 10^{-10}$  J of the total beam intensity is likely to be enough to heat the coil above transition temperate, and quench the superconducting magnets [7]. Such a chain reaction occurred in September 2008 when over 700 m of superconducting magnets were displaced by erroneously discharged liquid helium, caused by an electrical fault between two adjacent magnets [8]. The total cost of the damage was estimated at almost 20 million CHF, making a BLM system vital for minimising repair costs and ensuring the safe, long-term operation of the LHC.



Figure 3: Direct beam impact damage to vacuum component at ELBE, caused by a misaligned beam [9].

## 1.3 Project Aims

The overall aim of this project is to design a fast beam loss detector that is capable of identifying different magnitudes of loss. As requested by the industrial client at CERN, the necessary technical capabilities of this beam loss detector are:

- The ability to detect a single minimum ionising particle (MIP).
- The ability to detect up to  $1 \times 10^6$  MIPs per second.

- A time resolution  $< 25$  ns, to enable bunch-by-bunch beam loss measurements.
- The ability to operate in a radiation environment (an accumulated dose of  $< 1$  kGy).
- Has a surface area  $> 1$  cm<sup>2</sup>.
- Can be installed in the LHC tunnel in less than half a day.
- Powered by a single 230 V outlet.
- The ability to be controlled/readout using optical fibres (to connect to the network at CERN).
- Has a total cost of less than 10,000 CHF.

The most suitable components for a BLM system are chosen in section 3 and analysed against other detector types in sections 2 and 6. The theoretical performance of the suggested detector prototype is analysed in section 4 with respect to the criteria outlined above. Additionally, experimental methodology necessary to validate the expected results is discussed in section 5, followed by a consideration of further areas of research that would be necessary to optimise or actually install this device in the LHC tunnel in section 6.

## 2 Theoretical Background

### 2.1 Interaction of Charged Particles with Matter

When charged particles travel through matter they slow down, and hence lose energy. The study of this process is therefore of great importance for any measurement of the properties of different particles, and it is vital that detectors are built to interpret and distinguish between different levels of energy deposition caused by different charged particles travelling through matter. These charged particles lose their energy via physical processes such as:

- Coulomb interactions with electrons and nuclei.
- Emission of ionising radiation.
- Nuclear interactions.
- Cerenkov radiation emission.

Nuclear interactions are disregarded for the purposes of this report, as they affect heavier particles than those that are the focus of this report. Likewise, Cerenkov radiation emission is also ignored, since it is only emitted when a charged particle passes through a dielectric medium at a speed greater than the phase velocity of light in that medium [10].

A fast, charged particle may interact with the atomic nucleus of the atom, or most commonly the electrons, when travelling through a material. The force between a charged particle and an electron of a given atom, over

a radius  $r$ , can be given by the Coulomb force equation [11]. This force on the electron over time can result in an energy transfer to the electron, which is sometimes enough to liberate the electron from the atom and make it a free electron in a process called 'ionisation'. This electron's subsequent simplistic kinetic energy is given by,

$$KE = hv - \Phi \quad (1)$$

where  $h$  is Planck's constant,  $v$  is the velocity of the incoming particle and  $\Phi$  is the work function. An ionised electron acts like any other charged particle and will continue interacting with matter until it runs out of energy [12].

Fast beam collisions that result in an excitation or ionisation are hence considered 'inelastic collisions', and are the focus of BLM detector systems and this project.

Charged particles moving through matter emit energy via a form of electromagnetic radiation called 'bremsstrahlung', which is German for 'braking-radiation'. Bremsstrahlung is not a mono-energetic radiation, but instead consists of photons with energies from zero up to a maximum, depending on the kinetic energy of the particle [10].

The emission of bremsstrahlung from a charged particle is predicted by both quantum mechanics and classical physics to have an intensity proportional to the square of its acceleration. It can be therefore be deduced that:

- For two particles travelling in the same medium, the lighter one will emit a much greater amount of bremsstrahlung than heavier particles.
- More bremsstrahlung is emitted if the particle travels through a medium of higher atomic number  $Z$  than a comparative medium.

When a charged particle moves through a material it exerts Coulomb forces on many millions of atoms simultaneously. It is therefore impossible to calculate the energy loss by studying individual collisions and instead, an average energy loss is calculated per unit distance the particles can travel in a detector,  $dE/dx$ .

By considering only the energy lost due to ionisation, and assuming that all the atoms and their atomic electrons act independently, the average energy loss per unit distance travelled by a charged particle is given by the equation,

$$\frac{dE}{dx} = -\frac{4\pi e^3 N_A Z}{\beta^2 m c^2} \frac{1}{A} \left( \ln \left( \frac{2\beta^2 m c^2}{I} \right) - \ln(1 - \beta^2) - 1 \right) \quad (2)$$

where  $\beta$  refers to the relativistic velocity of the incident charged particle,  $I$  is the mean excitation potential,  $m c^2$  is the electron rest mass,  $Z$  is the atomic number of the medium and  $N_a$  is the Avogadro constant [13].

When this equation is plotted, for certain materials there will be a clear minimum energy loss which represents the energy deposited by minimum ionising particles.

## 2.2 Minimum Ionising Particles

A Minimum Ionising Particle (MIP) is a subatomic particle that has a mean energy loss rate close to the minimum possible, when interacting with any given material [14]. This is typically around  $2 \text{ MeV cm}^2/\text{g}$  [15], as shown in figure 4, which is a value that is taken as assumed throughout the rest of this report. A BLM detector requires a time resolution sufficient to detect these particles, as they are a good indication of the start of a fast beam loss event.

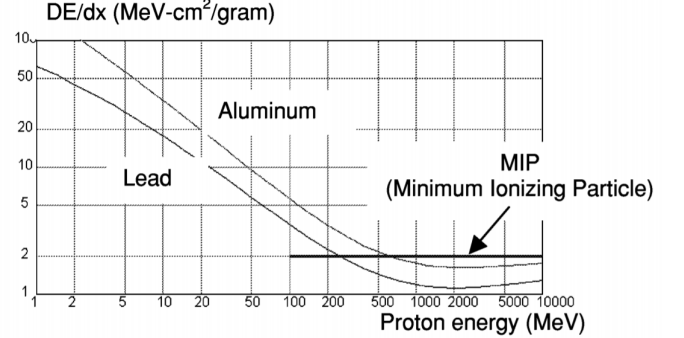


Figure 4: A graph showing the energy of a minimum ionising particle for two metals: lead and aluminium. The energy lost per unit distance of a minimum ionising particle is between the minimum point and the horizontal line; from the plot of equation 2 [16].

A range of detector types used to detect beam loss, and the different ways in which MIPs interact with different mediums, are explored further in section 2.4.

## 2.3 Key Principles of Fast Beam Loss Detection

A BLM system requires the ability to both detect lost particles and convert the measured pulse into a digital signal, to allow near-real time beam analysis and quick beam dumping when necessary. Consequently, the more data available on the location of the MIPs detected by the BLM system, the greater the ability to respond effectively and locate the machine component causing beam loss. When designing a detector, the ability to detect both a single MIP and detect up to  $1 \times 10^6$  MIPs per second is desirable, as this would give any BLM system both a high responsiveness to the start of a fast beam loss event, as well as the ability to measure its magnitude.

It is very difficult to know the exact efficiency of a BLM system due to the scattering effects caused by beam loss occurring at different locations. Some approximation of the BLM system efficiency can be found using 'Monte Carlo' programs where the signal produced by the detector is taken as proportional to the number of particles lost. An equation showing this relation is given as,

$$N = \frac{\text{Signal}}{\mathcal{E}} \quad (3)$$

where  $N$  is the number of lost particles,  $Signal$  is the signal given by the detector and  $\mathcal{E}$  is system efficiency [16]. This signal is then transmitted to and analysed by whichever read out system is used at CERN, via optical fibres.

An analysis of the different types of detectors already in use at CERN, and their suitability for the project brief, is undertaken below.

## 2.4 Current BLM Systems at CERN

### 2.4.1 Ionisation Chambers

Ionisation chambers are widely used in BLM systems due to their low cost and simple maintenance. The detector (shown in figure 2) is typically around 50 cm long, and consists of a series of parallel metallic electrodes separated by a gap of approximately 5 cm. The detector is also filled with gas such as  $N_2$  before a high voltage, up to several kV, is applied between the electrodes. Ionising particles travelling through the fluid will ionise atoms and produce electron-ion pairs, before the electric field caused by the applied voltage causes electrons and ions to drift in opposite directions. This will thus create a current that is proportional to the ionisation energy of incident particles. The collection time for the electrons is approximately  $0.3 \mu s$ , and about  $80 \mu s$  to collect the ions. Consequently, ionisation chambers cannot perform bunch-by-bunch analysis and hence will not be considered any further in this report [17].

### 2.4.2 Solid State Detectors

A solid state detector utilises the current generated by the movement of electron-hole pairs to measure beam loss. These electrons and holes are created and given energy upon the collision of a charged particle with the semi-conducting material, and are hence promoted to higher energy bands (the conduction band for electrons and the valence band for holes), as shown in figure 5.

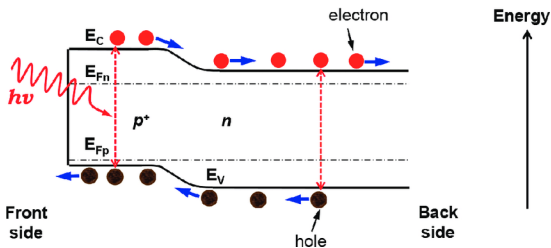


Figure 5: Schematic Energy Band Diagram Showing the Creation of Electron-Hole Pairs in n-type silicon by incident radiation [18].

When a voltage is applied across the semiconductor, these electrons and holes accelerate in different directions, and create a current proportional to the energy of the incident particles [19]. This voltage application is called 'biasing' the detector to make it behave like a diode as shown in figure 6. The direction and magnitude of this

bias can then be adjusted accordingly to change the noise or gain present in the device's current output, by varying the size of the band gap.

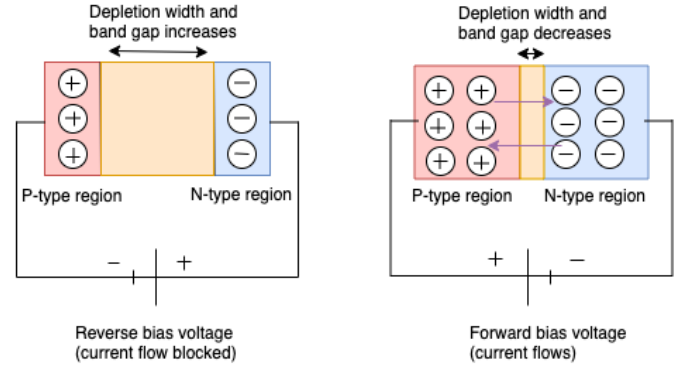


Figure 6: A hand drawn diagram showing the change in dark current by varying the depletion width.

The signal to noise ratio (SNR) of different semiconductors is largely dependent on the size of the band gap and applied voltage between the valence and conduction band. Thus, the smaller the 'barrier' to any prospective electron or hole jumping to a higher energy band, the greater the dark current that will be induced within the device. This dark current (which is the main source of system noise) thus represents the current present in photosensitive devices, even when no photons are incident upon it [18]. As well as operating a detector in reverse bias mode, semiconductors can also be 'doped' using other elements to increase the band gap size and hence increase the SNR.

The cheapest and most widely used semiconductor in solid state detectors is silicon, due to its relatively low cost and global abundance. The band gap of silicon is much smaller than 'wide band gap' semiconductors like diamond [20]. For this reason, silicon is usually doped by adding atoms of other elements to change the size of the material's band gap.

The small size of solid state detectors makes their installation easy and allows for precise, high resolution measurements of beam loss at key collimator junctions. The Compact Muon Solenoid (CMS) at CERN (shown in figure 7) employs thousands of strips of p-on-n type silicon semiconductor detectors, to detect any charged particles produced from the proton-proton collisions, occurring within it [21]. Detector arrays in the CMS that use SiPMs have a time resolution of up to 30–50 ns [22]. However, these arrays must be cooled to below  $0^\circ C$ , since the small band gap size creates a large dark current at room temperature [23].

Diamond based detectors are also widely used in BLM systems due to their wide band gap which gives rise to a very good SNR, as well as their ability to operate at higher temperatures [20]. Another appealing quality of diamond detectors is that they are far more resistant to radiation damage than silicon based detectors, by as much as an

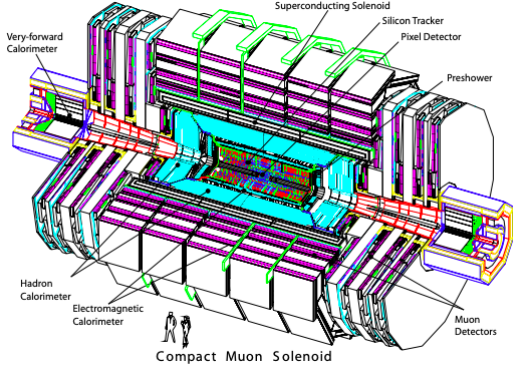


Figure 7: A schematic diagram of the CMS detector at CERN [21].

order of magnitude [24], which reduces the financial and time cost of re-installation in the radiation-hard environment of the LHC tunnel.

Four poly-crystalline chemical vapor deposition (pCVD) Diamond Beam Loss Monitors (DBLM), were mounted at a collimator section of the LHC in 2010 to test it's suitability for detecting fast beam loss. The detectors consisted of a  $10 \text{ mm}^2$  diamond substrate, of thickness 0.5 mm with a 200 nm thick gold electrode, of size  $8 \text{ mm}^2$  on each side as shown in figure 8. The detector is also mounted inside an aluminium box to provide it with radiation shielding [25].

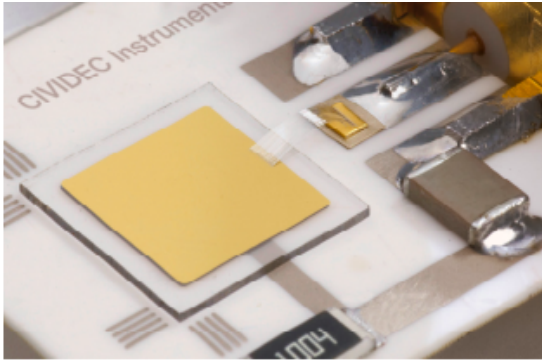


Figure 8: Picture of the top of the pCVD DBLM showing the gold electrode connected to the aluminium wire [25].

While a single pCVD detector has a time resolution of 615 ps, the whole pCVD system installed at CERN only has the ability to resolve single MIPs with a time resolution of less than 1 ns. This is due in part to the extensive series of cables needed to connect the detector to the read out system [25]. Despite this resolution being within the project brief, the greatest drawback of diamond detectors remains their up front cost which is considerable due to the rarity of high-quality diamonds and the length of the process that goes into the detector construction. Accordingly, the cost limit of 10,000 CHF was set by the client with the motivation of finding a cheaper alternative to diamond detectors that still enabled bunch-by-bunch beam

loss monitoring.

## 3 Prototype Detector Design

### 3.1 Scintillation Detectors

A scintillator is a material capable of scintillation, which is a process that causes the material to become luminescent once it has absorbed a particle of sufficient energy. Through collection and analysis of the photons emitted by the scintillator, information about the ionising particle that was incident on the material can be inferred. Fluorescence is responsible for the majority of the light emitted during scintillation [26].

Scintillation detectors can be made from a wide variety of materials, both organic and inorganic, which each have different properties. They are used in a range of scientific and industrial applications including medical imaging, ionising radiation detection and spectroscopy [27]. The use of a scintillation detector has some key advantages:

- It provides a relatively fast response time compared to other detector types.
- It is highly sensitive, as a large amount of photons are emitted when ionising energy is incident upon it. This will yield a good signal to noise ratio.

Solid inorganic and organic scintillation materials are the main consideration of this project, because of their sizes and availability. Their suitability is analysed below against the requirements of the project brief.

#### 3.1.1 Inorganic Scintillators

One of the most common inorganic crystals used for scintillation is Sodium Iodide (NaI), shown in figure 9. When doped with Thallium, it has a high light output (approximately 40,000 photons/MeV), due to its density and atomic number, but a slow output time of approximately  $1 \mu\text{s}$ . The output time is based on the rise and decay times of the scintillator which are the time taken for the signal to go from 10% to 90% of the maximum value [28], and the time taken for the signal to fall to  $1/e$  of the maximum [29], respectively. The output time is increased by a phenomenon called phosphorescence, which causes a delayed re-emission of energy from an excited state that is metastable. This re-emission occurs for a duration of the order of ms and the photons produced have larger wavelengths to those emitted via fluorescence [30].

Despite the high light output of inorganic scintillators, the output time is longer than the 25 ns required in this project to detect bunch-to-bunch beam loss. Consequently, for this reason and others; including the hygroscopic (humidity absorbing) nature of NaI, their sensitivity to temperature gradients, high phosphorescence and their cost, inorganic crystal scintillators are not considered any further in this report. [10].





Figure 9: Images of Thallium doped Sodium Iodide scintillators [31].

### 3.1.2 Organic Scintillators

Of all of the organic scintillators available, plastic scintillators are the most widely used. They are cheap to manufacture, and are easily shaped [30]. Plastic scintillators also have the benefit of producing an extremely fast signal, with response times ranging from a couple to tens of nanoseconds. This is because phosphorescence does not occur, due to the composition of the plastic scintillators [32]. This fast response time comes at the cost of light yield, which is normally only 20-30% of that emitted by NaI(Tl). However, plastic scintillators do not react with water and air, have a small temperature dependence and are radiation hard below roughly 100 kGy [33], all of which makes them an ideal candidate for a BLM system.

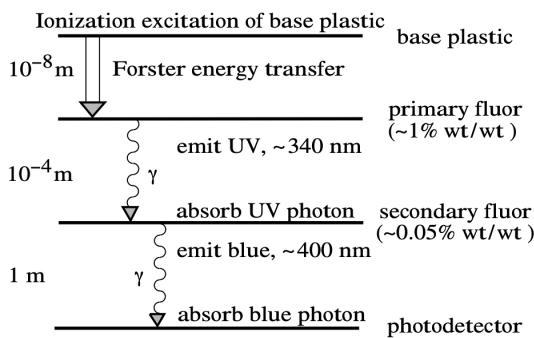


Figure 10: A simple diagram showing the process of emission from a plastic scintillator to a photodetector. The diagram shows the wavelength shifting through each layer of the scintillator [34].

The scintillation mechanism in an inorganic crystal is largely due to the structure of the crystal lattice. In an organic scintillator, the fluorescence arises from energy transitions of single molecules within the aromatic structure of the crystal [35]. The substance of the highest concentration in this structure is called the solvent, while other molecules are called solutes. Organic scintillators are typically comprised of a solvent and a solute (binary system) or a solvent, a primary solute and a secondary solute (tertiary system), with the secondary solute act-

ing as a wavelength-shifter. In a plastic scintillator, the most common solvents are polyvinyltoluene (PVT) and polystyrene. Highly fluorescent dyes are then used as solutes, which are known as 'fluors' [10].

When ionising radiation is incident on a plastic scintillator any free electrons will be excited to a higher energy state, as shown in figure 10. The electrons can then be excited to a higher vibrational energy state within that excited state before, per the Franck-Condon principle, relaxation occurs. This relaxation releases thermal energy, de-exciting the electron's vibrational state towards the ground of the excited state and causing its wavelength to be red-shifted, as shown in figure 11 [36].

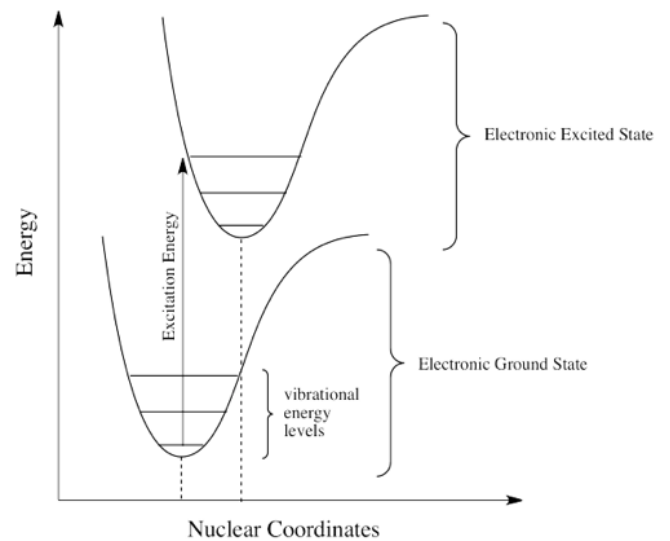


Figure 11: A graph showing the vibrational energy states alongside the electron energy states. De-excitation towards the lowest vibrational state causes red-shifting, highlighted by the dashed line to the increased nuclear coordinates [37].

The primary fluors in a scintillator are chosen to have similar energy states to that of the polymer (solvent) used, in order to allow for non-radiative energy transfer according to the the Förster resonance energy transfer mechanism between the polymer matrix to the primary fluor [38]. The fluor then has a low enough weight percentage, typically 1-5 wt.%, to eliminate direct ionisation from any incident energy. Accordingly, the electrons in the primary fluor will de-excite and release photons.

In a plastic scintillator, there is a secondary fluor of an extremely low weight percentage (0.005-0.5 wt.%), which is used to absorb these photons from the primary fluor and re-emit them at a longer wavelength. This will maximise photon output by reducing self-absorption by the primary fluor [39], causing emitted photons to now have a longer wavelength of approximately 400 nm, despite having initially been in the UV waveband following ionisation.

The fluorescent intensity of a plastic scintillator follows an exponential decay, convoluted with a Gaussian curve [32]. This fluorescence intensity  $I$  at time  $t$  is given

by,

$$I = I_0 e^{t/\tau} \quad (4)$$

where  $I_0$  is initial intensity and  $\tau$  is the decay constant.

Light output varies depending on material of the scintillator and the particle that is incident on the scintillator, and so an absolute unit was introduced to describe light yield on an absolute basis. This unit is called the 'MeVee' or 'electron-equivalent-energy'. The particle energy required to generate 1 MeVee of light is 1 MeV for fast electrons (figure 12). This number rises to several MeV for heavier particles, due to the reduced light yield per unit energy [26]. Throughout our calculations, we will assume that all incoming MIPs, from which we are calculating the capabilities of our detector, will have properties equivalent to the properties of an electron. This will allow us to use the standard MeVee units, and is a good approximation since an electron normally deposits an energy of around 2-3 MeV cm<sup>2</sup>/g [15].

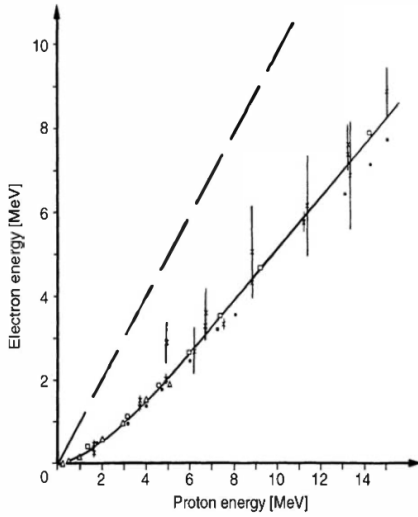


Figure 12: A graph showing light output (MeVee) as a function of incident proton energy (MeV). The dashed line shows the linearity of the light output against incident energy for an electron. The proton output is non-linear at lower energies. The graph also shows that light output from an incident electron is higher than that of a proton [26].

The light output of a scintillator can be described as the fluorescent energy emitted per unit path length  $dL/dx$ . This is proportional to energy loss for a charged particle shown by,

$$\frac{dL}{dx} = S \frac{dE}{dx} \quad (5)$$

where  $S$  is the normal scintillation efficiency. J.Birks adjusted this formula to account for ionisation quenching; this is when damaged molecules will absorb a fraction of the ionisation energy and not re-emit it, calculated using,

$$\frac{dL}{dx} = S \frac{dE}{dx} \left( 1 + kB \frac{dE}{dx} \right)^{-1} \quad (6)$$

known as Birks' formula. It is assumed that the density of damaged molecules along the path of the particle is directly proportional to the ionisation density. Hence,  $B(dE/dx)$  is the density of damaged molecules, with  $B$  as a proportionality constant. The fraction of these molecules that will lead to quenching is defined by  $k$ . This equation demonstrates that, for electrons, light output is linearly related to the incident energy [26].

## 3.2 Signal Digitisation and Amplification

In order for the emitted photons to be analysed, the signal needs to be amplified and converted to an electrical signal. This requires the use of a photomultiplier tube (PMT). The basic design of the PMT is a vacuum sealed vessel which contains a photocathode, an anode and a dynode array as shown in figure 13.

### 3.2.1 Photomultiplier Tubes

The photomultiplier tube provides highly sensitive photon detection, exceptionally low noise and ultra-fast response time [40]. This makes it an ideal component for use alongside a scintillator in a BLM system.

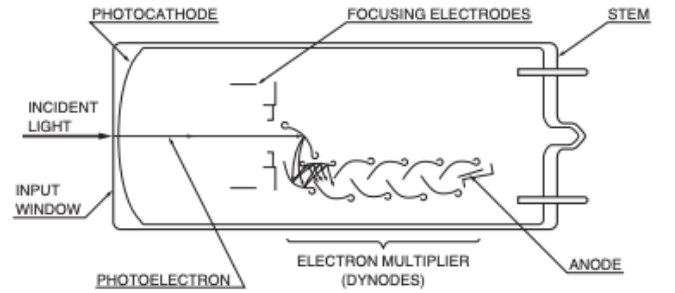


Figure 13: An internal diagram of a PMT utilising reflective dynode array [41].

### 3.2.2 Photocathode

The photocathode is a thin layer of photoemissive material which emits photoelectrons when photons are incident upon it via the photoelectric effect. During this process photons promote valence and conduction band electrons within the photo-emissive material, to energies high enough for them to escape into the vacuum of the PMT [42]. An applied voltage causes photoelectrons to accelerate towards the more positively charged anode.

Bialkali photocathodes are a common type of PMT due to their high radiant sensitivity and low dark current compared to other suitable photocathode materials [40], which is due largely to their low work functions. The cathode radiant sensitivity is the ratio of current to incident flux energy given by,

$$S_k = \frac{I_k}{\Phi_E} \quad (7)$$

where  $I_k$  is the corrected current measured over the cathode. The incident flux,  $\Phi_E$ , is calculated using,

$$\Phi_E = \frac{I_E A_C}{d^2} = \frac{N_\gamma h\nu}{td^2} \quad (8)$$

where  $I_E$  is the calibrated intensity of a photon source (LED),  $A_C$  is the area of the photocathode,  $d$  is the distance to the photon source,  $N_\gamma$  is the number of photons incident on the cathode and  $t$  is time [43].

Quantum efficiency as high as 43% has been achieved at peak wavelength for a class of photocathodes known as the ultra photocathode. The quantum efficiency of the photocathode corresponds to the fraction of incident photons that are converted into photoelectrons. Using equation 7, the quantum efficiency can be calculated,

$$\rho = \frac{S_{k\lambda} hc}{\lambda e} \quad (9)$$

where  $S_{k\lambda}$  is the cathode radiant sensitivity for a given wavelength,  $c$  is the speed of light in a vacuum,  $\lambda$  is the wavelength of incident light and  $e$  is the charge of an electron.

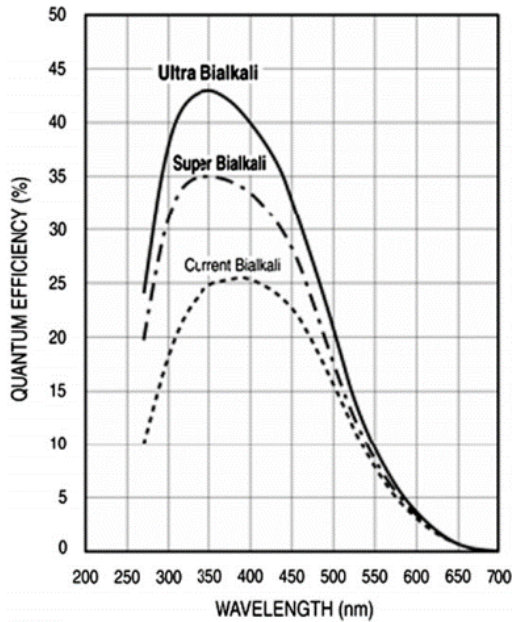


Figure 14: An approximate comparison of different bi-alkali photocathode types and their effect on quantum efficiency as a function of wavelength [40].

The quantum efficiency of a PMT is also dependant on the wavelength of incident photons and corresponding to photocathode peak emission wavelength as shown in figure 14. The higher the quantum efficiency, the greater the energy resolution [44].

The number of photoelectrons emitted by the photocathode can now be calculated using,

$$N_e = \rho N_\gamma \quad (10)$$

The number of photoelectrons can be further converted to give the current over the cathode, using,

$$I = \frac{N_e e}{t} \quad (11)$$

which will be used later.

### 3.2.3 Dynode Arrays and Signal Amplification

A dynode array is a series of structures within the PMT that are also covered with a photoemissive material. It is here that any increase in gain occurs, via the production of secondary emission electrons, in a chain reaction. Electrons produced at the cathode (as a result of incident photons), are accelerated towards a system of multiple dynodes by an inter-dynode potential difference, which increases the photoelectrons' kinetic energies [45]. Low energy secondary electrons are emitted from the emissive material surface, when photoelectrons of high enough energy are incident upon it. These secondary electrons then trigger a new round of photoelectron emission in the next dynode [46].

The outcome of this process is the production of many photoelectrons by the time the signal reaches the anode, which causes an increase in signal gain [47]. An increase in the inter-dynode potential and transit time of an electron enhances the multiplication effect, and therefore increases the gain further. However, any increase in transit time will lower the time resolution of the detector, as well as increase the time electrons can be influenced by external fields, and hence a compromise must be found [48].

Better dynode coating reduces the need for large numbers of, or high potential differences across dynodes. Boron-doped diamond, for example, has been demonstrated as an excellent, albeit expensive, secondary electron emitter [46]. This is due to diamond having a wide band-gap and low surface electron affinity; thus, it is used as a solid state detector in other, more expensive BLM systems [49].

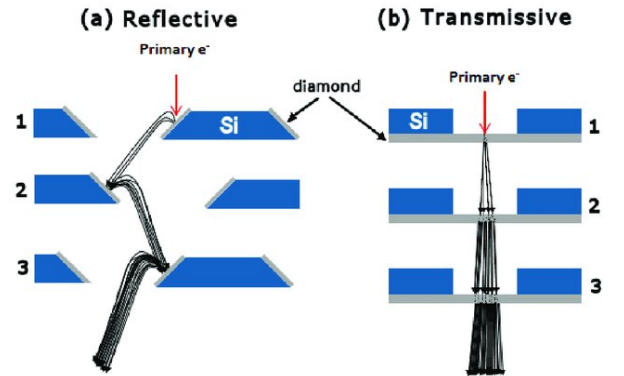


Figure 15: Difference in geometry of reflective dynode array (left) to transmissive dynode array (right) [46].

The geometrical setup of the dynode array also has important effects on the final PMT signal as shown in figure 15. A reflective array reflects electrons to each dynode,

whereas a transmissive array transmits electrons through the secondary emissive material. The transmissive setup results in improved quantum efficiency and lower pulse amplitude fluctuations [46]. A microchannel dynode array has high magnetic field immunity of up to 1.5 T without casings, excellent time characteristics and uniformity at the expense of cost and collection efficiency [46].

Available casings of shielding factor 1/10000 are sufficient to reduce up to 10 T down to a level acceptable level of 0.1 mT, meeting the lowest magnetic field immunity factor given by any dynode array. In other words, when using a casing of high magnetic shielding factor, external magnetic fields should have minimal effects on results, despite the transmission of the signal across the dynode array. From the final dynode, electrons are then accelerated toward the anode [50].

### 3.2.4 Anode Readout

The anode is responsible for collecting the large number of photoelectrons emitted by the final dynode. An oxidation reaction then occurs, resulting in a measurable electric charge in the connected circuit [51]. It is at the anode that most signals are measured and the overall characteristics of the PMT such as pulse width, rise time and gain are obtained.

There is a trade off between an increase in internal gain and fast rise times. The gain induced internally in the PMT is given by the ratio,

$$G = \frac{I_a}{I_k} \quad (12)$$

where  $I_a$  is the corrected current measured over the anode, generated at the cathode [43].

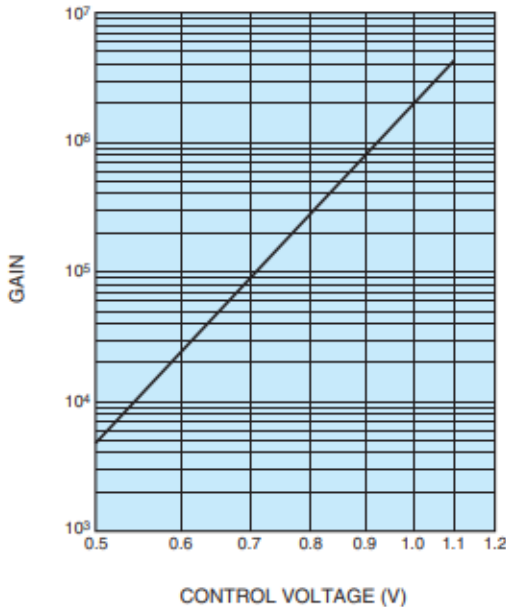


Figure 16: A graph showing the internal gain in a PMT as a function of increasing control voltages [41].

Efficiency of collection at the anode is dependant on characteristics such as the collection space and photoelectron travel time. In order to efficiently collect electrons, the shape and size of the anode must be considered. The radiant sensitivity of the anode given by,

$$S_a = \frac{I_a}{\Phi_E} \quad (13)$$

where  $\Phi_E$  is calculated using equation 8. Similar in theory to that of the photocathode, the anode is responsible for measuring current but at a larger magnitude due to the increase in gain at the dynodes [43].

Using given data sheets, theoretical values can be calculated for the expected current output signals over the cathode and anode, for an incident number of photons.

### 3.2.5 Dark Current and its Minimisation

For consistency within this report, the dark noise will be defined as the sum of all current caused by dark current sources. Dark current is a generation of current within the PMT in the absence of light. There are several causes for dark current, including thermionic emission from the photocathode and dynode, leakage current in the PMT, field emission and radiation from the environment [44]. Dark noise and its constituents can be calculated, using

$$I_{DarkNoise} = I_T + I_L + I_F \quad (14)$$

where  $I_T$  is dark current generated due to thermionic emission,  $I_L$  is dark current generated due to leakage current, and  $I_F$  is dark current generated due to field emission. Minimising these factors will produce the highest possible signal to noise ratio (the ratio of signal detected to background noise present).

Thermionic emission occurs as a result of thermal excitation of electrons at the photocathode and dynodes and therefore is strongly temperature dependant [52]. Leakage current provides a continuous component of dark current and occurs due to various factors, such as moisture or dirt between plug and pins or imperfections in insulation. A higher ohmic insulator further reduces the leakage current [45].

Field emission should also be considered as it can drastically shorten the life of a PMT and increase the dark current as shown in figure 17. Field emission occurs due to excessively high voltages within the PMT (figure 17), forcing the excitation of electrons from the dynodes. Operating at a voltage 20-30% less than the recommended input voltage ensures this effect is negligible [45]. External radiation from the environment can also be minimised by enclosing the PMT in a concrete box.

## 3.3 Time Characteristics

The full width half maximum (FWHM) is defined statistically as the distance between points on a curve at which the function reaches half its maximum value as shown in figure 18. This is applied to the current pulse detected



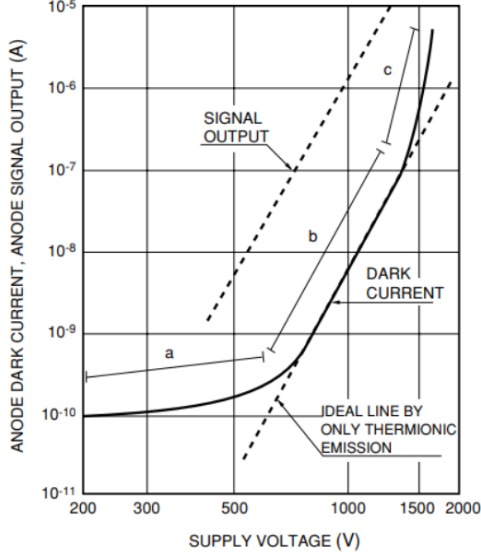


Figure 17: Effects of supply voltage on dark current. Low voltage region 'a', dark current contribution dominated by leakage current. Medium voltage region 'b', dark current contribution dominated by thermionic emission. High voltage region 'c', dark current contribution dominated by field emission [45].

over the anode, caused by incident photoelectrons and is given by,

$$t_w = \sqrt{(t_{w,a})^2 - (t_{w,l})^2} \quad (15)$$

where  $t_{w,l}$  is the FWHM of a light pulse and the  $t_{w,a}$  is the FWHM of the corresponding anode current pulse. Pulse width generally increases in magnitude with greater current pulses.

The rise time of an anode current pulse is the time difference between the start of a current signal and where the current signal reaches a maximum. This can be calculated by measuring the time required for the anode current to increase from 10% to 90% of its final value, in response to a light pulse, and approximately equals  $t_w$  [43].

The transit time is defined as the time interval between the arrival of a light pulse at the cathode and that of the corresponding current pulse at the anode. The transit time spread is the transit-time fluctuation observed when identical light pulses hit the same part of the cathode (figure 18). Consequently, the longer the path length, the more spread out multiple photoelectrons are likely to be, resulting in a slower rise time and pulse width [53].

The time resolution is defined as the FWHM of the probability distributions of the anode pulse arrival times, calculated using,

$$t_R = \frac{1}{\sqrt{N_{ei}}} \quad (16)$$

where  $N_{ei}$  is defined as the number of photoelectrons per pulse detected. Therefore, the FWHM of a current pulse, rise time and time resolution are all approximately equal to each other [43]. The shorter the transit time of photoelectrons, for example, the less influence the difference in

angle of trajectory has. Therefore, a shorter transit time results in a higher the probability that the photoelectrons will all be incident on the anode at the same time. Should all the photoelectrons be consistently incident at the same time, for example, a highly well defined probability density of very small FWHM will be seen (and excellent time resolution). A decrease in transit time of photoelectrons results in a smaller time resolution.

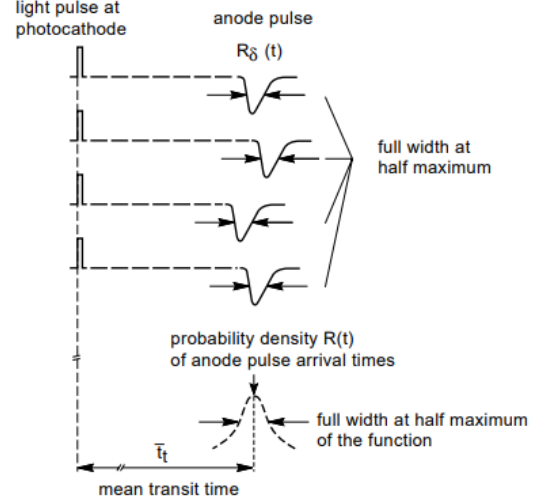


Figure 18: An illustration of the transit time, the FWHM of an anode current pulse (top) and the probability density of anode pulse arrival times (bottom) [43].

It is intuitive that as numbers of photoelectrons increase, the FWHM will also increase. The time resolution of a PMT is then inversely proportional to the rise time, shown in equation 16.

### 3.4 Final Prototype

Specific plastic scintillator and PMT models were chosen based on their suitability to the specifications that were required of the designed BLM system, as discussed in section 1.3. The peak wavelength output of the scintillator shown in figure 19 (391 nm) is also very close to the peak wavelength sensitivity of the PMT (400 nm), which will result in a large efficiency. Additional components have also been included to improve the design efficiency.

#### 3.4.1 Scintillator

The plastic scintillator deemed most suitable for this project is model EJ-228 from *Eljen Technology*.

The properties of this specific model, combined with the general properties of plastic scintillators mentioned in 3.1 (radiation hardness and inert nature), demonstrate why model EJ-228 is very suitable for use in a beam loss monitoring system.

Specification	Value
Light Output (% Anthracene)	67
Scintillation Efficiency (photons/MeV e <sup>-</sup> )	10,200
Wavelength of Maximum Emission (nm)	391
Rise Time (ns)	0.5
Decay Time (ns)	1.4
Pulse Width FWHM (ns)	1.2
Polymer Base	PVT
Refractive Index	1.58
Vapour Pressure	Vacuum Compatible
Temperature Range (°C)	-20-60
Softening Temperature (°C)	75

Table 1: The properties and composition of the scintillator model EJ-228, most notably the rise and decay times, the refractive index, the spectral light output as a percentage of Anthracene and the efficiency [54].

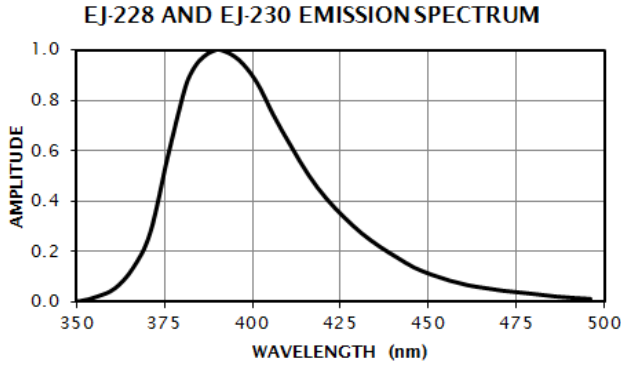


Figure 19: The emission spectrum of the scintillator model EJ-228, clearly showing that the maximum emission is at wavelength 391 nm [54].

### 3.4.2 Photo Multiplier Tube

The PMT most suitable for this project is Model H13229P-210, produced by **Hamamatsu**.

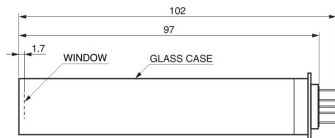


Figure 20: Side view of the PMT [55].

Specification	Value
Transit Time (ns)	0.57
Active Area (cm <sup>2</sup> )	0.502
Peak Sensitivity Wavelength (nm)	400
Input Voltage (v)	2.8-5.5
Max Input Current (mA)	2.7
Max Output Current (μA)	100
Recommended Voltage Adj. Range (V)	0.5-1.1
Temperature Range (°C)	5-50

Table 2: A table of all relevant functional properties of the PMT chosen [55].

All client specifications are met by the chosen device, including the ability to measure bunches of  $1 \times 10^6$  MIPs. A P-type PMT is used as it is well suited for photon counting, with very low dark noise. An ultra bialkali photocathode provides radiant sensitivity of  $130 \text{ mAW}^{-1}$  corresponding to an average quantum efficiency of 41.23% at the optimal (400nm) wavelength.

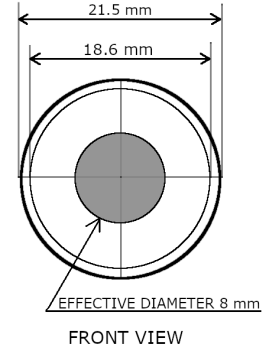


Figure 21: Front view of the PMT (hand drawn). The effective diameter of the circular tube is 8 mm, therefore its effective area is  $0.502 \text{ cm}^2$ .

A peak sensitivity at wavelength 400 nm corresponds to our chosen scintillator (figure 22). A dark count of  $50 \text{ s}^{-1}$  results in minimal dark noise. An internal gain of  $10^{5.2}$  is exhibited at a control voltage of 0.8 V as shown in figure 16. An excellent rise time of 0.57 ns, coupled with the ability to operate in a vacuum. The PMT photocathode has a diameter of 8 mm resulting in an active area of  $0.502 \text{ cm}^2$ . PMT window transmittance of 93% is high and does not include Q2-3067 Optical Couplant.

The window is made of borosilicate glass of approximate refractive index 1.52 [56]. It is assumed with stated optical grease the PMT window has a transmittance of approximately 96%.

Figure 1: Spectral response

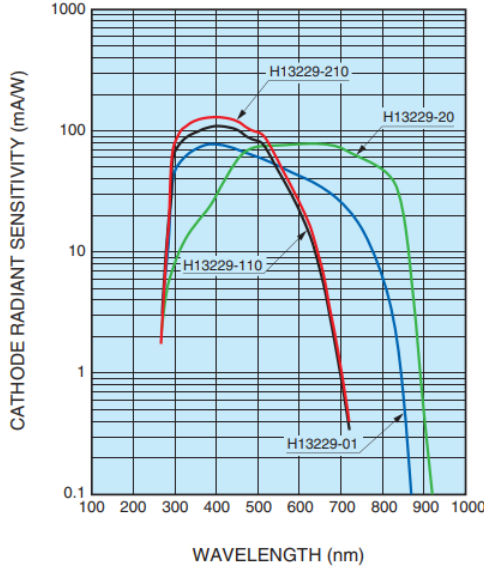


Figure 22: Spectral response of chosen PMT (red line) showing peak sensitivity wavelength at 400 nm [55].

### 3.5 Necessary Experimental Accessories

A power supply unit is included to ensure the systems ability to connect to a 230 V mains supply. This will step 230 V down to a 5 V input suitable for the PMT module [57].

Optical grease is to be placed between the scintillator and PMT window. Q2-3067 Optical Couplant of refractive index close to 1.52 can be used. Without data, it is assumed that ,based off other experiments, the transmittance will increase from 93% without optical grease, to 96% with the optical grease [58].

A magnetic shield casing of shielding factor 1/10000 must be applied in order to reduce magnetic fields of up to 10 T effecting efficiency. If the PMT is subject to higher magnetic fields, a mesh or micro-channel plate array is recommended [59].

### 3.6 Cost Sheet

Component	Approximate Cost per Unit (CHF)
Scintillator (EJ-228)	300
Bi-alkali PMT (H13229P-210)	1800
Optical Grease	545
Mag. Field Casing	1000
<b>Total</b>	<b>3650</b>

Table 3: A table outlining the approximate costs of the key components of the detector. This excludes tax and transport costs.

As can be seen from table 3, the proposed prototype components are well within the 10,000 CHF budget.

## 4 Expected Performance

In the sections below, the expected performance of the selected components, including the expected time resolutions and currents generated by different numbers of incident MIPs, is presented. These calculations are based on data provided by the manufacturers, and are laid out thoroughly alongside all the equations used in the appendix in section 8. It must be taken into consideration however that, due to being unable to verify our methodology in a laboratory setting, all results listed below are theoretical and hence lots of approximations and assumptions regarding optimal conditions have been made, in lieu of actual data.

### 4.1 Detector Efficiency

All calculations of the capabilities of the detector design will assume an overall detection efficiency of 10%, which is calculated using equation 18. This calculation combines the scintillator and PMT quantum efficiency factors (10,200 photons/MeV  $e^-$  [54] and 41.23% [55]), the 25% efficiency reduction due to the active area difference between the PMT and scintillator, and the PMT window transmittance (96% including optical grease). The impact of dark noise is considered negligible for the purpose of this calculation of the maximum efficiency of the detector design. Ways to improve the BLM system efficiency are explored in section 6.2, with calculations again taking place in the appendix in section 8.2.

Since the EJ – 228 scintillator produces 10,200 photons/MeV  $e^-$  this will mean that a single MIP produces approximately 20,400 photons in the scintillator, since an MIP is assumed to deposit approximately 2 MeV  $cm^2/g$  and the scintillator is assumed to be 1  $cm^3$  in volume. This calculation of 20,400 photons then needs to be multiplied by the calculated detector efficiency of 10% to give the number of photons incident on the PMT cathode. This value of 2040 photons reaching the cathode per incoming MIP will be used in all subsequent calculations of the time resolution and expected current readings generated by different numbers of incident MIPs.

### 4.2 Theoretical Detection Results

Using a control voltage of 0.8 V over the PMT will result in a gain of order  $10^{5.2}$ . A single MIP per 1 second results in a corrected current over the anode,  $I_a$ , of 51.7 pA. At the same control voltage,  $1 \times 10^6$  MIPs per second results in a corrected current over the anode of 51.7  $\mu A$ . At this gain, both current results are within the saturation limit of 100  $\mu A$  of the PMT [55]. By rearranging equation 21 and using the saturation limit of the PMT, a minimum number of 1 MIP and a maximum number of  $1.9 \times 10^6$  MIPs are calculated as detectable at the chosen

voltage. It is difficult, however, to estimate the lowest energy MIP that could be detected by the detector. The amount of background noise is hard to theorise and experimental verification is required to determine the minimum readable output signal current. However, the PMT has a typical dark count rate of  $50 \text{ s}^{-1}$  [55], which is very small.

### 4.3 Operating Conditions

These conditions should guarantee the best performance from the detector:

- Radiation - The output current should not be affected in the LHC operation environment.
- Magnetic Field - The prototype should be able to operate effectively in a magnetic field of up to 10 T strength.
- Temperature - Optimal efficiency is achieved between  $5^\circ\text{C}$  to  $40^\circ\text{C}$ . The signal output will drop exponentially beyond this point.
- Pressure - The prototype works most efficiently at atmospheric pressure.
- Orientation - Maximum efficiency will be achieved when the MIP is incident on the detector perpendicularly to the surface.

The efficiency of the PMT is related to its peak wavelength sensitivity (400 nm) which is in the PMT data sheet and shown in figure 22. A significant drop off of cathode radiant sensitivity is seen at approximately  $\pm 100$  nm from peak wavelength sensitivity. Although figure 22 does not account for the use of optical grease, it is nevertheless still expected that the efficiency of the detector will suffer beyond  $\pm 50$  nm from peak wavelength sensitivity due to the reduced efficiency of the PMT. The scintillator emission spectrum is given in figure 19. Over 80% of the emitted light will fall between the wavelengths of 375 nm and 425 nm, and a further 95% of light falls between the wavelengths of 350 nm and 450 nm. Since 95% of the emission spectrum of the scintillator falls within the region before the drop off in efficiency of the PMT, an optimum PMT efficiency of 41.23% at 400 nm was assumed for all theoretical calculations.

The PMT has an operating range of  $5^\circ\text{C}$ – $50^\circ\text{C}$ , however, beyond room temperature ( $20^\circ\text{C}$ ), the effects of dark current are more significant and need further investigation during experimental validation of calculated results [55]. The scintillator has an operating temperature of  $-20^\circ\text{C}$ – $60^\circ\text{C}$ . This leads to a recommended operating temperature of as close to  $5^\circ\text{C}$  as possible.

The efficiency is expected to represent a sinusoidal waveform when plotted against the angle of incident MIPs from 0 to  $\pi$ . Maximum efficiency should occur when the beam is perpendicular to the detector. Radiation does not have a considerable effect on the light output of the scintillator until accumulated dose is higher than 0.1 MGys. At 0.9 MGy, scintillator light output is still about 95%

of the maximum [60]. The effects of radiation over time require further practical investigation.

### 4.4 Corrected System Rise Time

For a single photoelectron, the PMT has a rise time and FWHM of approximately 0.57 ns. For a single MIP, the system has a corrected rise time and approximate FWHM of 25.7 ns measured over the anode. For  $1 \times 10^6$  MIPs, the system has a corrected rise time of 25.7  $\mu\text{s}$ . The detector therefore has the ability to detect both a single MIP and  $1 \times 10^6$  MIPs per second.

### 4.5 Time Resolution for Bunch-by-Bunch BLM

In accordance with the above calculations, a time resolution of 35.0 ps is expected for bunch-by-bunch detection, for  $8.01 \times 10^{17}$  MeV bunches produced within the LHC. A thorough calculation is shown in the appendix section 8.6.

## 5 Experimental Verification

The theoretical performance of the suggested prototype has now been determined using data from the manufacturers in section 4, but further practical experimentation will be required to validate these expectations. In this section, the tests that could be done to verify the performance of this prototype will be detailed.

### 5.1 Component Setup

The chosen EJ–228 plastic scintillator of surface area  $1 \text{ cm}^2$ , is positioned perpendicular to, and as flush as possible against, a current output PMT module. Optical grease is then applied to the glass window of the PMT. A step-down power supply unit connects to the mains and input of the PMT. Some form of signal readout, such as an oscilloscope, is connected to the output of the PMT. The entire system is then enclosed in a concrete box of thickness 0.25 m. A proposed setup can be seen in figure 23.

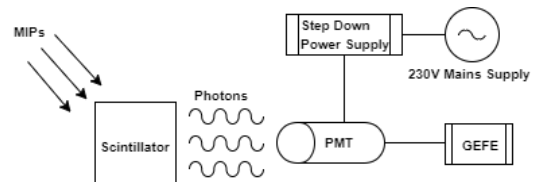


Figure 23: Diagram showing the prototype setup and the process leading to a signal.

## 5.2 Calibration of the Signal Digitisation System

Initial calibration of detection system must be performed before any reliable data collection. A measure of dark noise generated at the PMT must be determined and deducted from any results gathered. Calibration can be conducted using an already calibrated LED in place of the scintillator. The LED acts as a continuous source of MIPs or a scintillator with 100% efficiency. Once the PMT is calibrated, it can be used to calibrate the scintillator.

### 5.2.1 PMT Dark Noise Correction

To measure the dark noise signal, as much light and external radiation must be removed from the photocathode as possible. No measurements should be taken until the system has been left in total darkness for more than 30 minutes. The use of dark rooms and thick concrete bricks with high water to cement ratio is also advised.

Leakage current can be minimised by ensuring wiring insulation is both highly ohmic and attached correctly, while also keeping humidity low. Field effects can be minimised by keeping the PMT control voltage within the recommended range [55]. To get an average dark current reading, the temperature must remain as close to experiment operating temperature throughout the experiment (room temperature). The dark current measured across the anode can then be subtracted from all subsequent calculations.

### 5.2.2 Coincidence Detection

In order to further reduce the effects of dark noise a second detector can be placed within the concrete box, with a thin sheet of lead separating the individual detectors. Muons detected by the first detector will propagate through the lead and reach the second detector, resulting in MIP detection by both detectors within a time frame of microseconds, due to the propagation speeds of a muon. This will confirm that a MIP has been detected and not a dark noise signal, by reducing the probability the detected pulse is random noise. Combining these techniques will minimise dark noise to near negligible for this experiment.

### 5.2.3 PMT Calibration Using a Pulse Generator

The constant number of photons incident on the PMT and emitted by a LED can be calculated using equation 17. For simplicity, it is assumed the area of the LED and PMT are equal and are flush against each other, ensuring all photons are collected by the PMT. The current over the cathode is measured using a resistor and a voltmeter. The change in volts over the resistor can be used to give the current over the photocathode using  $V = IR$ . Taking the dark noise, measured previously, away from the measured cathode current will give a noise corrected photocathode current. Otherwise, using equation 7 and

data sheet values, a photocurrent over the cathode can be calculated theoretically.

The quantum efficiency of the photocathode can now be calculated using equation 9. Using the number of photons incident to the photocathode and quantum efficiency stated on the PMT data sheet, the number of photoelectrons emitted by the photocathode can also be calculated theoretically using equation 10.

By using similar methods discussed for measuring the current over the cathode, a value for the current over the anode can be obtained. Otherwise, using a gain of  $10^{5.2}$  which is observed at a control voltage of 0.8 V and shown in figure 16, the current over the anode to be calculated theoretically using equation 13.

Detected electrons can then be compared to the number of incident photons. Should measured values agree with calculations, after considering factors effecting PMT efficiency, this concludes PMT calibration.

## 5.3 Calibration of Scintillator Detector using Cosmic Rays

Once the scintillator is fully calibrated, the entire system can be considered fully calibrated and the number of muons detected by the system should be close to the average 20 muons per second found at sea level. This can be confirmed by positioning the detector at the top of the Wills Physics Laboratory in Bristol, to avoid any stray radiation from other experiments and taking readings. This elevation is under 100 m and so will have minimal variance from accepted sea level data.

Using the PMT calibrated previously, the scintillator can now be calibrated. To calibrate the scintillator for MIP detection, the number of photons emitted must be consistent with the amount of energy incident from a single MIP. The number of photons emitted per muon is calculated using the data sheet [54] for energies of 2 MeV  $cm^2/g$  per incident muon. The calibrated PMT can now be used to measure the number of photons incident on the photocathode.

A theoretical value for current produced as a result of incident muons on the scintillator can be determined using equation 22. Should the PMT detect the correct number of photons emitted by the scintillator after all efficiency corrections, the system calibration is complete.

The prototype detector is now fully calibrated and ready to begin data collection. Measuring the number of MIPs detected as a function of time for the initial prototype setup, will give a set of control data, which can be used for analysis and comparison of future data sets.

## 5.4 Pulse Generator to Simulate LHC Bunches

The setup discussed is now fully calibrated and has shown to be capable of detecting a single ionising particle in muon cosmic ray form. Now, the setup must prove capable of detecting bunches 25 ns apart. To do this, a UV

emitting LED is connected to a pulse generator which is capable of pulsing a number of photons corresponding to  $1.1 \times 10^{10}$  MIPs, at 25 ns intervals. The equipment should be set up as shown in figure 23, with the UV LED around 0.1 m away from the face of the scintillator. For a continuous time, let the pulse generator pulse the LED at 25 ns intervals, recording the time it takes for the detector to process the signal and the PMT to record the signal. If the number of signals is equal to the number of pulses, and the signal current is consistent with the number/energy of UV photons reaching the scintillator face, the detector has the capability to detect bunch-by-bunch beam loss in under 25 ns.

## 5.5 Optimal Conditions and Efficiency

### 5.5.1 Minimum MIPs Detectable

The number of muons incident on the detector at sea level is on average, 1 every 20 seconds. This should allow the efficiency of single MIP detection to be easily determined. Should the detector operate at 100% efficiency, 180 MIPs should be detected in one hour. Extending this method with a longer time frame will reduce error, and allow a more accurate comparison.

### 5.5.2 Maximum MIPs Detectable

The maximum number of MIPs detectable by a scintillator is much greater than  $1 \times 10^6$  per second, leaving the upper limits of the PMT to be investigated. To measure an upper limit of the number of MIPs detectable by the PMT, gradually increase the number of photons emitted by the pulse generator, until saturation occurs and the signal no longer increases with an increase in incident photons.

### 5.5.3 Effects of Magnetic Field

To investigate the effects on the setup from a change in magnetic field the system can be subject to an increasing magnetic field, alongside a measurements of the anode current. The change in anode current as a function of increasing magnetic field gives the PMTs efficiency at different magnetic fields. Magnetic field casings of varying shielding factors can also be applied, to see how efficiency increases. The magnetic field of the Earth is typically reduced to the nano Tesla range as casings are applied.

### 5.5.4 Orientation

Measuring the number of MIPs detected, as a function of their incident angle on scintillator, will allow a determination of optimal and minimal detector angles for MIP detection. The PMT will need to remain flush against the back of the scintillator throughout. The detector will begin at  $\phi = 0$  rad and then can be rotated through an angle of  $\phi = \pi$  rad at increments of 0.004 rad (approximately 0.25 degrees). The data collected can be analysed

to determine the angle for maximum and minimum MIP detection.

## 6 Discussion

Due to the results obtained in section 4 being theoretical in nature and relying on many approximations, rigorous error analysis of their precision or accuracy is impossible. Given the number of components used, it is speculated that the margins of error for the results obtained will be relatively high. These results should be repeatable according to the methodology detailed in section 5, although any results obtained in a laboratory setting, with their greater accuracy and reliability, are likely to deviate from those calculated in section 4.

### 6.1 Evaluation of the Chosen Detection System Against Project Brief

According to the theoretical calculations based on component specifications, the designed detector setup would meet the project requirements. The calculations of corrected rise times of 25.7 ns for 1 MIP and 25.7  $\mu$ s for  $1 \times 10^6$  in section 8.5 indicate that the detector's time resolution is likely to be able to detect  $1 \times 10^6$  MIPs per second in accordance with the project brief. Additionally, the calculated time resolution of 35.0 ps in section 8.6 would allow for bunch-by-bunch beam loss measurements to be conducted in less than 25 ns per the client's criteria.

The primary technical requirements for use of the detector in a BLM system at CERN were thus considered to be met. Due to an inability to collect results, it will be discussed below in sections 6.2, 6.5 and 6.7 whether the secondary aims relating to the actual installation of the detector system at CERN have also been satisfied. The total cost of the design was 3650 CHF, which is within the given budget.

### 6.2 Maximum Efficiency and Theoretical Optimal Conditions

An overall efficiency of 10% was calculated for the detector system in section 5, due to the PMT only having an active area about 25% that of the scintillator. This difference in active area size was difficult to avoid, due to the lack of production of larger PMT photocathode areas. Efficiency could be increased to as much as 39.6% if the active areas of the scintillator and PMT were of equal surface area and one side of the scintillator was covered with reflective paint to improve photon transmission, as calculated in section 8.2. However, the use of reflective paint will increase time resolution which is undesirable for BLM purposes. The upper limit of 39.6% detector efficiency is largely due to the photocathode of the chosen PMT having a quantum efficiency of 41.23%. This is nevertheless a high value compared to non bi-alkali photocathodes,



meaning the use of different PMTs is therefore unlikely to achieve a larger efficiency. This 41.23 % is then further limited by the PMT window transmittance, which is just below 100% transmittance efficiency. For these reasons, the efficiency of the detector design is limited to 39.6%, even under optimal conditions.

To ensure a maximum efficiency, environmental conditions should be carefully considered. The scintillator has an efficiency of 95% at 60°C [54]. Any increase above this temperature would further reduce its efficiency, before it ceases to function at 75°C. In contrast, the maximum and minimum operating temperature of the PMT is 50°C and 5°C, respectively [55]. To achieve the lowest thermionic dark current emission, the PMT should be kept at low temperatures. Therefore, if the system as a whole is operated in the same temperature environment, a temperature of 5°C is recommended as detailed in section 4. If the detectors are installed on the outside of the LHC where the temperature is approximately 34°C near the superconducting guiding magnets [61], an additional cooling system is likely to be required.

Accordingly, a vacuum would most likely be the best controllable environment to place the detector in, since its lack of a medium and humidity would also reduce transit times and leakage current, as well as allowing temperature control. Both the scintillator and the PMT are rated for operation in a vacuum, down to a pressure limit of 0.001 Pa for the PMT [55]. A common component used to achieve vacuum conditions is the 'Roman pot' shown in figure 24.

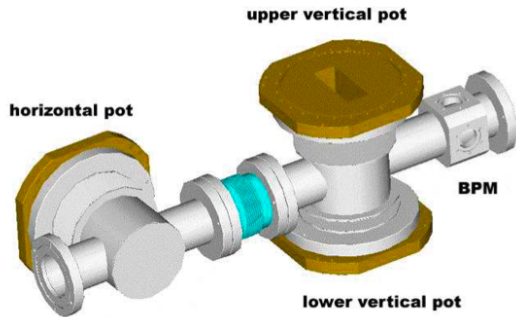


Figure 24: Basic diagram of a Roman pot [62].

A Roman pot usually consists of a vertical cylinder containing a secondary and primary vacuum space which is attached to the beam line through bellows and allows the movement of a detector into the primary vacuum, closer to the beam [62]. This will improve detector sensitivity, allowing it to detect even beam losses of small angular beam deviation [63]. The Roman pot typically operates between 25°C – 40°C, as this is the typical temperature exhibited in it during a proton-proton beam collision [64]. This high temperature range is likely to impact the output efficiency of the detector and requires further practical investigation. However, with the use of a

cooling system, the vacuum environment could be maintained at the optimum 5°C mentioned above, although this will increase system installation time and cost.

### 6.3 Improving System Time Resolution

Despite the expected time resolution of the detector calculated in section 4 being within the requirements of the project brief, there are many potential unaccounted for causes of reduced efficiency and hence, decreased time resolution. To improve the detector's time resolution, an increased number of photoelectrons must be incident on the anode in a smaller time frame. This can be achieved by increasing the component transmission efficiency according to the calculations for using optical fibres, reflective paint and equal active areas made in section 8.2, or by shortening the signal transit time. Another way to achieve this would be to increase the internal gain of the PMT, through coating the dynodes with materials of higher secondary electron emission coefficients. One such material is GaP(Cs), which has a secondary emission coefficient of greater than 60 photoelectrons per incident energy of 1 keV, with a linear increase according to the amount of incident energy [45]. An increase in gain would thus increase the number of photoelectrons incident on the anode.

One way to reduce the transit time of photoelectrons in the PMT is to use microchannel plate (MCP) dynode arrays, which have a very small transit times between them (approximately 400 ps). Since such high numbers of photoelectrons are incident on the anode in a small time frame, MCPs with rise times as low as 150 ps have been achieved. Furthermore, MCP dynode arrays greatly reduce the effects of stray magnetic fields, reducing the dark current present in the PMT [45]. When this decrease in transit time is couple with a a higher number of photoelectrons incident over the anode, a larger pulse will be produced in a smaller time frame, increasing the time resolution of the device.

The additional effect of the necessary additional read out infrastructure on the transit time of the signal and time resolution of the BLM system will be briefly discussed in section 6.7.

### 6.4 Improving the Signal to Noise Ratio

Improving the signal produced by the detector, while simultaneously reducing background noise, will results in a higher signal to noise ratio (SNR). The simplest way to increase the size of the produced signal, other than increasing the efficiency as previously mentioned, is to increase the gain of the PMT by using a model that has more expensive photoemissive materials such as GaP(Cs) coated over its photocathode and dynodes. Additionally, should time resolution be disregarded, increasing the number of dynodes and transit time of photoelectrons would also increase the signal gain, as would using a scintillator with a higher photon output per MeV, such as the inorganic

type discussed in section 3.1.

The most effective way of reducing background noise is operating the PMT at lower temperatures. This requires using a cooling system for the Roman pots as mentioned in section 6.2. This would result in a reduction of thermionic emission from photoemissive surfaces and hence lower the dark current present in the detector, which is likely to be the main source of noise in the LHC. Keeping the applied voltage toward the lower end of recommended range which, for this PMT, is between 20-30% of the maximum recommended voltage stated in [55], will also reduce field emission noise. This low applied voltage of around 0.77 V will increase the lifetime of the PMT but also lower the gain, therefore its overall effect on the SNR requires further practical investigation.

Secondary detector infrastructure can also contribute significantly to the noise in any BLM system, which has led to the ongoing upgrade of the standard coaxial cables at the LHC. This upgrade uses an optical fibre network to connect components together where appropriate, and transmits signals to the computers on the surface. Optical fibres produce less interference and stray electromagnetic radiation than coaxial cables due to their lower resistivity, and are hence preferable for use in BLM systems. They will also reduce the transit time of a signal and increase the time resolution of the BLM system compared to coaxial cables, due to their high refractive index meaning that the signal travels close to light speed. Additionally, consideration of the grounding location of the voltage system is necessary, since grounding to an area that has stray radiation or vibrations will cause noise to be generated that interferes with the beam loss signal [65]. All connection and components should also be cleaned thoroughly before use to ensure they are dirt and moisture free.

Due to the depth of the LHC underground, it can be assumed that external radiation will have a minimal effect on the detection system, and radiation shielding is therefore likely to be unnecessary and unlikely to affect the SNR, especially considering the radiation hardness of the components detailed in section 6.5. Additionally, any increase in the thickness of the scintillator used in this report would result in more energy deposited and more photons produced per incident MIP. However, this increase in signal size would come at the expense of increased signal transit time, therefore is not a useful avenue of exploration or calculation, given the time resolution requirements of the project brief.

## 6.5 Radiation Hardness and Life Expectancy

A key aim of this project was to develop a detector able to withstand up to 1 kGy dose of accumulated radiation. At accumulated doses of 0.9 MGy, the scintillator light output is still about 95% of the maximum [60]. Beyond this level, the scintillator should be replaced to maximise detector efficiency. While the scintillator used is radiation hard and well suited for BLM systems, should the PMT

not be shielded from 100% of the radiation from particle beams, its efficiency is likely to deteriorate. This may require the PMT to have further radiation shielding, such as the concrete of thickness greater than 0.25 m detailed in section 5. Alternatively, the client may wish to line the system with ice or water due to both substances' high hydrogen content providing excellent protection against all non-heavy ions. Although these substances are cheap, they are perhaps not eminently practical, and further research into other types of shielding such as an aluminium box should be undertaken in a laboratory setting.

With minimal radiation incident on the PMT and regular warm up before usage, the PMT can be expected to achieve a lifetime exceeding several thousand hours of operating time when recommended operating voltages are applied [66]. However, it is notoriously difficult to predict a PMT's life expectancy, and for this reason a practical measurement of the effects of different accumulated dosages on each component will need to be made in a laboratory setting, alongside regular physical checks of the BLM system after installation into the LHC.

## 6.6 Critical Appraisal Against Current CERN Detectors

One of the primary motivations for this project from the client's perspective was the design of a BLM system capable of the requirement criteria, that is also cheaper than the diamond detectors currently installed at collimator sections, to detect fast beam loss. Although their wide band gap ensures a low dark current and a high signal to noise ratio, the high price of diamonds makes their widespread use difficult and not ideal considering the number of detectors normally employed in a BLM system at the LHC.

The other leading BLM detector design that has already been installed at certain CERN experiments is the **Timepix3 hybrid pixel detector** produced by the international Medipix Collaboration. The Timepix3 detector, four of which were installed at the LHC in 2017, contains a chip with a matrix of over 65,000  $55\ \mu\text{m} \times 55\ \mu\text{m}$  pixels of p-n diodes. This allows for a measurement of the direction in which a beam loss event occurs, by examining which pixels have a charge induced in them, above the threshold voltage of around 500 eV. This threshold therefore allows the detection of particles that have an energy greater than 1.8 keV when they hit the sensor, allowing for high resolution detection of MIPs. The detector also has the ability to measure an MIP's charge, by timing how long the induced voltage remains above the threshold [67]. The operation of the Timepix3 is therefore not dissimilar to how photosensitive film functions in an optical camera. The chip itself digitises any information about charge being induced in the pixels, above the threshold level. It then transmits this to a computer which can analyse the data and quickly trigger a beam dump, if it is determined that a fast beam loss event is underway.



The Timepix3 device has a time resolution of 1.56 ns for a single MIP [68], which is far faster than the detector detailed in this report which only has a corrected rise time of 25.7 ns for a single MIP. This, coupled with the ability to extract information about the magnitude of charge passing through the detector by measuring the time the signal generated is over the set threshold, allows for extremely accurate information about the direction, duration and composition of any beam loss that occurs. This level of specificity is beyond the project brief, and budget, despite the promise this solid state detection technology shows.

## 6.7 Further Areas of Research

This report details how to construct a prototype particle detector in a laboratory setting. For actual installation into the LHC however, a consideration of the necessary components to carry the signal generated by the PMT up to the surface and into computers away from the radiation environment is necessary. A system using an Analogue to Digital Converter (ADC), connected to a Field Programmable Gate Array (FPGA) and then to optical fibres is one of the most common and practical ways to achieve this. This readout system is employed by the Timepix 3 BLM [67].

An initial investigation suggests that the use of a 'Giga Bit Transceiver based Expandable Front-End' (GEFE) shown in figure 25 is likely to also be required for signal digitisation. The GEFE is a multi-purpose, radiation hard (up to 750 krad [69]) FPGA based card, that is used for transmitting data from the front-end (near the beamline) to the back-end (radiation safe environment). It takes advantage of the 'versatile link' already at CERN, which is an extensive series of optical fibres that run through the facility [70] that provides a 4.8 Gbps, bi-directional optical link [69]. The impact of this extensive optical fibre network on signal transit time, dark current and time resolution of the BLM also requires further verification in a laboratory setting.



Figure 25: Image of GEFE v1 [69].

The GEFE, shown in figure 25, can be expanded with an ADC mezzanine card to convert analogue signals from the BLM detector, and then connected via the versatile link to a VFC-HD general-purpose digital acquisition card which is located on the surface [71].

All of these components, as well as the optical fibres will extend the installation time required for the BLM system considerably, especially if there are no pre-installed

components to plug into. It is probably safe to assume however, that at least an optical fibre network and Roman pots should be pre-existing and available for use, meaning that the required install time of less than half a day is most likely still achievable. Therefore, the increase in total transit time of the signal from the detector to the computer system is likely to instead be the greatest issue which faces any further project design that aims to also achieve the requirements of the project brief.

## 7 Conclusion

In accordance with the project brief, a BLM system has been designed that meets the client's stated requirements, is within the budget, and can be installed in less than half a day. Theoretical calculations have proven the system's ability to detect a single MIP, one million MIPs within a second and bunch-by-bunch loss in less than 25 ns. Further areas of research have also been highlighted, including suggestions of potential upgrades to constituents of the system that would improve its performance should results obtained by the methodology laid out in section 5 vary from values calculated in section 4.

From these calculations, it was determined that the chosen detector set up can detect 1 MIP and  $1 \times 10^6$  MIPs in 25.7 ns and 25.7  $\mu$ s, respectively. The time resolution was found to be 35 ps, over an active scintillator area of 1 cm<sup>2</sup>. It has therefore been concluded that relatively cheap scintillation materials and PMT detectors are perfectly suitable for fast MIP detection up to 1.9 million MIPs. It has been further concluded that the detection system stated is perfectly suited for LHC applications of bunch-by-bunch measurements within the necessary time resolution of less than 25 ns. Estimations, ways to investigate and suggested corrections of error for variables, like the transit time spread of current pulses detected over the anode, have subsequently been detailed in sections 4 and 6.

Furthermore, suggestions of various ways to improve the signal to noise ratio, efficiency and time resolution of the device are also detailed in sections 5 and 6. This involves the discussion and analysis of additional system accessories that would be required to optimise the detector's performance and provide a signal readable by a computer after its actual installation into the LHC.

## 8 Appendix

### 8.1 PMT Theoretical Calibration

The number of photons emitted by the LED can be calculated using,

$$E = IVt = N_{LED}h\nu \quad (17)$$

where  $E$  is electrical energy supplied,  $I$  is current,  $V$  is voltage supplied,  $t$  is time,  $h$  is Planck's constant,  $\nu$  is frequency of light and  $N_{LED}$  is the number of photons emitted by the LED.

### 8.2 Efficiency Calculations

It is assumed all efficiencies are calculated at system optimal conditions. The efficiency of the chosen prototype is calculated using,

$$\mathcal{E}_{Tot} = \mathcal{E}_{Area}\mathcal{E}_{PMT}\mathcal{E}_{WT}\mathcal{E}_{Half} = 10.0\% \quad (18)$$

where  $\mathcal{E}_{Area}$  is due to area difference between the scintillator and PMT,  $\mathcal{E}_{PMT}$  is the quantum efficiency of the PMT,  $\mathcal{E}_{WT}$  is due to the window transmittance with optical grease, and  $\mathcal{E}_{Half}$  is due to photon emission radiating away from one side of the scintillator.

The efficiency of the prototype should reflective paint and optical fibre bundles be used is calculated using,

$$\mathcal{E}_{Tot} = \mathcal{E}_{OFB}\mathcal{E}_{PMT}\mathcal{E}_{WT} = 25.7\% \quad (19)$$

where  $\mathcal{E}_{OFB}$  is the transmittance efficiency of the optical fibre bundle.

The efficiency of the prototype should reflective paint and equal active areas flush against each other be used, is given by,

$$\mathcal{E}_{Tot} = \mathcal{E}_{PMT}\mathcal{E}_{WT} = 39.6\% \quad (20)$$

giving the maximum possible efficiency when using the chosen scintillator and PMT. Any prototype that uses reflective paint will result in a wider FWHM pulse width.

### 8.3 Theoretical Detection Results

Subbing in  $\mathcal{E}_{Tot}$  for the chosen efficiency setup will give the expected corrected current measured over the anode using the equations below. Using a control voltage of 0.8 V results in a gain of  $10^{5.2}$ . This gain is used throughout to ensure linearity. It is denoted  $G$ . The dark count rate for the PMT is 50 per second [55], which results in a negligible dark noise and will ensure calculated currents are distinguishable.

The current measured over the anode as a result of a number of MIPs of  $2 \text{ MeV cm}^2/\text{g}$  incident on the detection system is given by,

$$I_a = \frac{N_{MIPs}N_{Tot\gamma}\mathcal{E}_{Tot}Q_eG}{t} \quad (21)$$

where  $N_{MIPs}$  is the number of MIPs incident on the scintillator,  $\mathcal{E}_{Area}$  is the efficiency as a result of difference in scintillator and photocathode area,  $\mathcal{E}_{PMT}$  is the efficiency of the PMT,  $Q_e$  is the charge of an electron and  $N_{Tot\gamma}$  is the number of photons emitted by the scintillator per  $2\text{MeV}$ .

Using a control voltage of 0.8 V results in a gain of  $10^{5.2}$ . A single MIP per 1 second results in a corrected current over the anode of,  $I_a=51.7 \text{ pA}$ . At the same control voltage,  $1 \times 10^6$  MIPs per second results in a corrected current over the anode of  $I_a=51.7 \mu\text{A}$ .

The current measured over the anode as a result of a number of muons, of average energy dissipated  $2 \text{ MeV cm}^2/\text{g}$ , incident on the detection system is given by,

$$I_a = \frac{N_{muons}N_{Tot\gamma}\mathcal{E}_{Tot}Q_eG}{t} \quad (22)$$

where  $N_{muons}$  is the number of muons incident on the scintillator.

Using a control voltage of 0.8 V results in a gain of  $10^{5.2}$ . A single muon per 20 second results in a corrected current over the anode of,  $I_a=2.6 \text{ pA}$ . A single muon per 1 second results in a corrected current over the anode of,  $I_a=51.7 \text{ pA}$ . At the same control voltage,  $1 \times 10^6$  muons per second results in a corrected current over the anode of  $I_a=51.7 \mu\text{A}$ .

## 8.4 Theoretical Detection Results With Maximum Efficiency Setup

The results in this section are a result of using the maximum possible efficiency for the chosen prototype. The only loss of efficiency is due to chosen PMT characteristics such as quantum efficiency and window transmittance. Equal active areas and reflective paint are used to ensure the maximum number of photons are incident on the PMT. An overall detection efficiency of 39.6% is used for this setup.

The current measured over the anode as a result of a number of MIPs of 2 MeV cm<sup>2</sup>/g incident on the detection system is given by,

$$I_a = \frac{N_{MIPs} N_{Tot\gamma} \mathcal{E}_{Tot} Q_e G}{t} \quad (23)$$

A single MIP per 1 second results in a corrected current over the anode of,  $I_a=204.9$  pA.  $1 \times 10^6$  MIPs per second results in a corrected current over the anode of  $I_a=204.8$   $\mu$ A. This current is greater than the max output current signal capabilities of the chosen PMT. For detection systems of this efficiency, control voltage should be adjusted.

The current measured over the anode as a result of a number of muons of 2 MeV cm<sup>2</sup>/g incident on the detection system is given by,

$$I_a = \frac{N_{muons} N_{Tot\gamma} \mathcal{E}_{Tot} Q_e G}{t} \quad (24)$$

A single muon per 20 second results in a corrected current over the anode of,  $I_a=10.2$  pA. A single muon per 1 second results in a corrected current over the anode of,  $I_a=204.9$  pA.  $1 \times 10^6$  muons per second results in a corrected current over the anode of  $I_a=204.9$   $\mu$ A.

## 8.5 Corrected System Rise Time

It is assumed that the FWHM calculated using equation (16) is approximately equal to rise time. The total pulse width is expected to increase with increasing numbers of photoelectrons. A correction is made for numbers of photoelectrons greater than 1 to account for the nonlinear movement of incident photoelectrons. This is referred to throughout as the corrected rise time. The corrected rise time can be considered further analysis and is calculated mainly to aid in understanding the time resolution.

The number of photons produced from the scintillator as a result of incident MIPs of 2 MeV is calculated using,

$$N_e = N_{MIPs} N_{Tot\gamma} \mathcal{E}_{Tot} \quad (25)$$

which can be used to calculate the corrected rise time of the scintillator. For a single MIP, 20400 photons are produced. For  $1 \times 10^6$  MIPs,  $2.04 \times 10^{10}$  photons are produced.

The number of photoelectrons produced at the photocathode as a result of incident photons is calculated using,

$$N_e = N_{MIPs} N_{Tot\gamma} \mathcal{E}_{Tot} \quad (26)$$

which can be used to calculate the corrected rise time of the PMT. For a single MIP, 2040 photoelectrons are produced. For  $1 \times 10^6$  MIPs,  $2.04 \times 10^9$  photoelectrons are produced.

The rise time of the system is measured over the anode. The corrected rise time of the system is calculated approximately using,

$$t_T = \sqrt{N_e} t_w \quad (27)$$

where the chosen PMT has a rise time of 0.57 ns for a single electron. Hence, for a single MIP, the system has a corrected rise time 25.7 ns measured over the anode. For  $1 \times 10^6$  MIPs, the system has a corrected rise time of 25.7  $\mu$ s.

## 8.6 Time Resolution for Bunch-by-Bunch Beam Loss Measurements

Each beam at the LHC consists of 2808 bunches with total beam energies of 360MJ. Therefore, since 360MJ corresponds to  $2.25 \times 10^{21}$  MeV each bunch has an energy of  $8.01 \times 10^{17}$  MeV. The number of photoelectrons produced as a result of this energy being incident on the system is calculated using,

$$N_e = E_{Bunch} N_{Photon} \mathcal{E}_{Tot} \quad (28)$$

where  $N_{Photon}$  is the number of photons emitted per MeV. For the chosen scintillator, this is constant at 10200 photons. Therefore, the number of photoelectrons emitted per incident bunch is  $8.2 \times 10^{20}$ .

Using the number of photoelectrons emitted, the time resolution can then be calculated, using,

$$R_t = \frac{1}{\sqrt{N_e}} \quad (29)$$

results in a time resolution of 35.0 ps. This is within the specification.

## References

- [1] Bin Guo. *Measurement of the Top Quark Pair Production Cross Section and an in-situ B-tagging efficiency Calibration with ATLAS in pp collisions at  $\sqrt{s}=7$  TeV in Dilepton Final States*. PhD thesis, Toronto U., 2011.
- [2] Alexandre Arbey, Marco Battaglia, Abdelhak Djouadi, and Farvah Mahmoudi. The Higgs sector of the phenomenological MSSM in the light of the Higgs boson discovery. *Journal of High Energy Physics*, 2012(9):107, 2012.
- [3] RW Assmann, M Magistris, O Aberle, M Mayer, F Ruggiero, JM Jiménez, S Calatroni, A Ferrari, G Bellodi, I Kurochkin, et al. The final collimation system for the lh. Technical report, 2006.
- [4] R. Schmidt. Machine Protection. (arXiv:1601.05207. arXiv:1601.05207):23 p, Jan 2016. 23 pages, contribution to the CAS - CERN Accelerator School: Advanced Accelerator Physics Course, Trondheim, Norway, 18-29 Aug 2013.
- [5] Kay Wittenburg. Beam loss monitoring and control. In *Proceedings of EPAC*, pages 109–113, 2002.
- [6] L Bottura. Magnet quench 101. *arXiv preprint arXiv:1401.3927*, 2014.
- [7] Lyndon Evans and Philip Bryant. LHC machine. *Journal of instrumentation*, 3(08):S08001, 2008.
- [8] M Bajko, L Rossi, R Schmidt, P Strubin, P Cruikshank, P Limon, R Denz, S Fehér, L Tavian, M Koratzinos, et al. Report of the Task Force on the Incident of 19th September 2008 at the LHC. Technical report, 2009.
- [9] Kay Wittenburg. Beam loss monitors. *arXiv preprint arXiv:2005.06522*, 2020.
- [10] Nicholas Tsoulfanidis. *Measurement and detection of radiation*. CRC press, 2010.
- [11] Carl R Seubert, Laura A Stiles, and Hanspeter Schaub. Effective coulomb force modeling for spacecraft in earth orbit plasmas. *Advances in Space Research*, 54(2):209–220, 2014.
- [12] Stephen Klassen. The photoelectric effect: Reconstructing the story for the physics classroom. *Science & Education*, 20(7):719–731, 2011.
- [13] P Lecoq. Scintillation detectors for charged particles and photons. *Landolt Börnstein*, 21:45, 2011.
- [14] Donald E Groom and SR Klein. Passage of particles through matter. *The European Physical Journal C-Particles and Fields*, 15(1):163–173, 2000.
- [15] H Ammi, R Zemih, S Mammeri, and M Allab. Mean excitation energies extracted from stopping power measurements of protons in polymers by using the modified bethe-bloch formula. *Nuclear Instruments and Methods in Physics Research Section B: Beam Interactions with Materials and Atoms*, 230(1-4):68–72, 2005.
- [16] Robert E Shafer. A tutorial on beam loss monitoring. In *AIP Conference Proceedings*, volume 648, pages 44–58. American Institute of Physics, 2002.
- [17] Bernd Dehning, E Effinger, J Emery, G Ferioli, G Guaglio, EB Holzer, Daniel Kramer, L Ponce, V Prieto, M Stockner, et al. The lh beam loss measurement system. In *2007 IEEE Particle Accelerator Conference (PAC)*, pages 4192–4194. IEEE, 2007.
- [18] Yuguo Tao and Ajeet Rohatgi. High-efficiency front junction n-type crystalline silicon solar cells. *Nanostructured Solar Cells*, page 93, 2017.
- [19] Jingtian Fang, Mahmud Reaz, Stephanie L Weeden-Wright, Ronald D Schrimpf, Robert A Reed, Robert A Weller, Massimo V Fischetti, and Sokrates T Pantelides. Understanding the average electron-hole pair-creation energy in silicon and germanium based on full-band monte carlo simulations. *IEEE Transactions on Nuclear Science*, 66(1):444–451, 2018.
- [20] Leon M Tolbert, Burak Ozpineci, S Kamrul Islam, and Madhu S Chinthavali. Wide bandgap semiconductors for utility applications. *semiconductors*, 1:3, 2003.
- [21] CMS Collaboration. The CMS experiment at the CERN LHC. 2008.
- [22] Marco Lucchini, CMS Collaboration, et al. Development of the CMS MIP timing detector. *Nuclear Instruments and Methods in Physics Research Section A: Accelerators, Spectrometers, Detectors and Associated Equipment*, 958:162090, 2020.
- [23] D Attree, B Anderson, EC Anderssen, V Akhnazarov, RJ Apsimon, P Barclay, LE Batchelor, RL Bates, M Battistin, J Bendotti, et al. The evaporative cooling system for the ATLAS inner detector. *Journal of Instrumentation*, 3(07):P07003, 2008.
- [24] Wim De Boer, Johannes Bol, Alex Furgeri, Steffen Müller, Christian Sander, Eleni Berdermann, Michal Pomorski, and Mika Huhtinen. Radiation hardness of diamond and silicon sensors compared. *physica status solidi (a)*, 204(9):3004–3010, 2007.
- [25] E Griesmayer, E Effinger, H Pernegger, D Dobos, and B Dehning. A fast CVD diamond beam loss monitor for LHC. In *Conf. Proc.*, volume 11, page MOPD41, 2011.

- [26] Glenn F Knoll. *Radiation detection and measurement*. John Wiley & Sons, 2010.
- [27] Cheol Ho Lee, Jaebum Son, Tae-Hoon Kim, and Yong Kyun Kim. Characteristics of plastic scintillators fabricated by a polymerization reaction. *Nuclear Engineering and Technology*, 49(3):592–597, 2017.
- [28] P Tarif and T Bourbie. Experimental comparison between spectral ratio and rise time techniques for attenuation measurement. *Geophysical prospecting*, 35(6):668–680, 1987.
- [29] P. Lecoq, A. Gektin, and M. Korzhik. *Inorganic Scintillators for Detector Systems: Physical Principles and Crystal Engineering*. Particle Acceleration and Detection. Springer International Publishing, 2016.
- [30] W.R. Leo. *Techniques for Nuclear and Particle Physics Experiments: A How-to Approach*. Springer Berlin Heidelberg, 2012.
- [31] Advatech UK Ltd. NaI(Tl)-Sodium Iodide (Tl). [https://www.advatech-uk.co.uk/nai\\_t1.html](https://www.advatech-uk.co.uk/nai_t1.html). (Accessed on 13-04-2021).
- [32] Chung Yau and Elton Ho. Cosmic ray muon detection using NaI detectors and plastic scintillators. *American Institute of Physics*, 3, 2008.
- [33] Advatech UK Ltd. Plastic scintillators. [https://www.advatech-uk.co.uk/scintillators\\_plastic.html](https://www.advatech-uk.co.uk/scintillators_plastic.html). (Accessed on 13-04-2021).
- [34] Roger Rusack. Seeing the Light Lecture 2 - The Physics of Detectors . <https://indico.cern.ch/event/518648/attachments/1271861/1885030/Lecture3-Scintillators-Light-Detection.pptx.pdf>. (Accessed on 17-04-2021).
- [35] T.A. Abrajano, B. Yan, and V. O'Malley. 11.13 - high molecular weight petrogenic and pyrogenic hydrocarbons in aquatic environments. In Heinrich D. Holland and Karl K. Turekian, editors, *Treatise on Geochemistry (Second Edition)*, pages 481–509. Elsevier, Oxford, second edition edition, 2014.
- [36] ROBERT K Swank. Characteristics of scintillators. *Annual review of nuclear science*, 4(1):111–140, 1954.
- [37] LibreTexts. Singlet and triplet excited state. [https://chem.libretexts.org/Bookshelves/Physical\\_and\\_Theoretical\\_Chemistry\\_Textbook\\_Maps/Map%3A\\_Physical\\_Chemistry\\_for\\_the\\_Biosciences\\_\(Chang\)/14%3A\\_Spectroscopy/14.7%3A\\_Fluorescence\\_and\\_Phosphorescence](https://chem.libretexts.org/Bookshelves/Physical_and_Theoretical_Chemistry_Textbook_Maps/Map%3A_Physical_Chemistry_for_the_Biosciences_(Chang)/14%3A_Spectroscopy/14.7%3A_Fluorescence_and_Phosphorescence). (Accessed on 14-04-2021).
- [38] Harekrushna Sahoo. Förster resonance energy transfer—A spectroscopic nanoruler: Principle and applications. *Journal of Photochemistry and Photobiology C: Photochemistry Reviews*, 12(1):20–30, 2011.
- [39] Tibor Jacob Hajagos, Chao Liu, Nerine J Cherepy, and Qibing Pei. High-z sensitized plastic scintillators: A review. *Advanced Materials*, 30(27):1706956, 2018.
- [40] Kimitsugu Nakamura, Yasumasa Hamana, Yoshihiro Ishigami, and Toshikazu Matsui. Latest bialkali photocathode with ultra high sensitivity. *Nuclear Instruments and Methods in Physics Research Section A: Accelerators, Spectrometers, Detectors and Associated Equipment*, 623(1):276–278, 2010.
- [41] Hamamatsu. *Photomultiplier Tubes And Assemblies For Scintillation Counting High Energy Physics*.
- [42] JB Pendry. Theory of photoemission. *Surface Science*, 57(2):679–705, 1976.
- [43] SO Flyckt and Carole Marmonier. Photomultiplier tubes: principles & applications.[online] 2002.
- [44] Xiang-Cui Lei, Yue-Kun Heng, Sen Qian, Jing-Kai Xia, Shu-Lin Liu, Zhi Wu, Bao-Jun Yan, Mei-Hang Xu, Zheng Wang, Xiao-Nan Li, et al. Evaluation of new large area pmt with high quantum efficiency. *Chinese Physics C*, 40(2):026002, 2016.
- [45] OF NIR. Photomultiplier tubes.
- [46] Shu Xia Tao, Hong Wah Chan, and Harry Van der Graaf. Secondary electron emission materials for transmission dynodes in novel photomultipliers: A review. *Materials*, 9(12):1017, 2016.
- [47] Abraham Pais. Einstein and the quantum theory. *Reviews of modern physics*, 51(4):863, 1979.
- [48] Jiyuan Zheng, Lai Wang, Xingzhao Wu, Zhibiao Hao, Changzheng Sun, Bing Xiong, Yi Luo, Yanjun Han, Jian Wang, Hongtao Li, et al. A pmt-like high gain avalanche photodiode based on gan/aln periodically stacked structure. *Applied Physics Letters*, 109(24):241105, 2016.
- [49] Raquel Maria Amaro Vaz. *Studies of the secondary electron emission from diamond films*. PhD thesis, University of Bristol, 2013.
- [50] AG Wright. *The photomultiplier handbook*. Oxford University Press, 2017.
- [51] Vladimir S Bagotsky. *Fundamentals of electrochemistry*, volume 44. John Wiley & Sons, 2005.
- [52] Ralf Widenhorn, Morley M Blouke, Alexander Weber, Armin Rest, and Erik Bodegom. Temperature dependence of dark current in a ccd. In *Sensors and Camera Systems for Scientific, Industrial, and Digital Photography Applications III*, volume 4669, pages 193–201. International Society for Optics and Photonics, 2002.

- [53] James S Milnes and J Howorth. Picosecond time response characteristics of microchannel plate pmt detectors. In *26th International Congress on High-Speed Photography and Photonics*, volume 5580, pages 730–740. International Society for Optics and Photonics, 2005.
- [54] Eljen Technology. Fast timing plastic scintillator ej-228, ej-230. [https://eljentechnology.com/images/products/data\\_sheets/EJ-228\\_EJ-230.pdf](https://eljentechnology.com/images/products/data_sheets/EJ-228_EJ-230.pdf). (Accessed on 15/02/2021).
- [55] Photosensor Module H13229 Series/H14211 Series. [https://www.hamamatsu.com/resources/pdf/etd/H13229\\_H14211\\_TPM01086E.pdf](https://www.hamamatsu.com/resources/pdf/etd/H13229_H14211_TPM01086E.pdf), 10 2018. (Accessed on 16/02/2021).
- [56] Schott. Borosilicate Glass Properties. <https://www.schott.com/d/tubing/9a0f5126-6e35-43bd-bf2a-349912caf9f2/schott-algae-brochure-borosilicate.pdf>. (Accessed on 26-04-2021).
- [57] Hamamatsu. Power Supply Unit C7169/C10709 Series. [https://www.hamamatsu.com/resources/pdf/etd/C7169\\_C10709\\_TACC1049E.pdf](https://www.hamamatsu.com/resources/pdf/etd/C7169_C10709_TACC1049E.pdf). (Accessed on 23/03/2021).
- [58] Dow Corning. DOW CORNING® Q2-3067 Optical couplant. [https://www.paisleyproducts.com/content/files/content/tds/AVDCQ23067\\_tds\\_9\\_9\\_2014.pdf](https://www.paisleyproducts.com/content/files/content/tds/AVDCQ23067_tds_9_9_2014.pdf). (Accessed on 24-04-2021).
- [59] Magnetic shield cases e989 series. [https://www.hamamatsu.com/resources/pdf/etd/PMT\\_120\\_en.pdf?fbclid=IwAR0WhcRgAJVKrGNok6m8VLj0UARhdZ8aY6iqNi-CZ33sWPX4Mhch-C1WMBUK](https://www.hamamatsu.com/resources/pdf/etd/PMT_120_en.pdf?fbclid=IwAR0WhcRgAJVKrGNok6m8VLj0UARhdZ8aY6iqNi-CZ33sWPX4Mhch-C1WMBUK), 2012. (Accessed on 25/04/2021).
- [60] Harshna Jivan. Radiation hardness of plastic scintillators for the Tile Calorimeter of the ATLAS detector. [https://indico.cern.ch/event/471180/contributions/1990765/attachments/1225962/1794756/HJivan\\_HEPP2016\\_presentation.pdf](https://indico.cern.ch/event/471180/contributions/1990765/attachments/1225962/1794756/HJivan_HEPP2016_presentation.pdf). (Accessed on 22-04-2021).
- [61] MA Pimenta dos Santos. Thermal analysis of one LHC tunnel octant. Technical report, 2000.
- [62] Giovanni Anelli, G Antchev, P Aspell, V Avati, MG Bagliesi, V Berardi, M Berretti, V Boccone, U Bottigli, M Bozzo, et al. The TOTEM experiment at the CERN Large Hadron Collider. *Journal of Instrumentation*, 3(08):S08007, 2008.
- [63] Marco Oriunno, Mario Deile, Karsten Eggert, Jean-Michel Lacroix, Serge Jean Mathot, Elias Philippe Noschis, Roger Perret, Ernst Radermacher, and Genaro Ruggiero. The roman pot for the lhc. In *Proceedings of EPAC*, volume 6, pages 562–564, 2006.
- [64] F Ravotti. Beam-induced heating in the TOTEM Roman Pot detectors at the LHC. Technical report, 2012.
- [65] Alan James Bell. *The Design & Construction of the Beam Scintillation Counter for CMS: A Thesis Submitted in Partial Fulfillment of the Requirements for the Degree of Master of Science in Physics at the University of Canterbury*. PhD thesis, University of Canterbury, 2008.
- [66] Burle Industries. Life expectancy of PMT. [https://psec.uchicago.edu/links/Photomultiplier\\_Handbook.pdf](https://psec.uchicago.edu/links/Photomultiplier_Handbook.pdf). (Accessed on 26/04/2021).
- [67] Hampus Sandberg, W Bertsche, D Bodart, B Dehning, S Gibson, S Levasseur, K Satou, G Schneider, JW Storey, and R Veness. First use of Timepix3 hybrid pixel detectors in ultra-high vacuum for beam profile measurements. *Journal of Instrumentation*, 14(01):C01013, 2019.
- [68] Erik Frojdh, M Campbell, M De Gaspari, S Kulis, X Llopart, T Poikela, and L Tlustos. Timepix3: first measurements and characterization of a hybrid-pixel detector working in event driven mode. *Journal of Instrumentation*, 10(01):C01039, 2015.
- [69] Manoel Barros Marin, A. Boccardi, C. Godichal, Jose Gonzalez, T. Lefevre, Thomas Levens, and B. Szuk. The Giga Bit Transceiver based Expandable Front-End (GEFE)—a new radiation tolerant acquisition system for beam instrumentation. *Journal of Instrumentation*, 11:C02062–C02062, 02 2016.
- [70] Mohammad Amin Shoaie, Stefano Meroli, Simao Machado, and Daniel Ricci. Evolution of optical fibre cabling components at CERN: Performance and technology trends analysis. *Optical Fiber Technology*, 42:69–74, 2018.
- [71] Manfred Wendt, A Boccardi, T Bogey, I Degl’Innocenti, C Moran Guizan, Verena Kain, M Barros Marin, and Athanasios Topaloudis. Upgrade of the CERN SPS Beam Position Measurement System. In *9th Int. Particle Accelerator Conf.(IPAC’18), Vancouver, BC, Canada, April 29-May 4, 2018*, pages 2047–2050. JACOW Publishing, Geneva, Switzerland, 2018.